ECOLE POLYTECHNIQUE

CENTRE DE MATHÉMATIQUES APPLIQUÉES

UMR CNRS 7641

91128 PALAISEAU CEDEX (FRANCE). Tél: 01 69 33 41 50. Fax: 01 69 33 30 11
http://www.cmap.polytechnique.fr/

Impact of Volume Viscosity on a Shock/Hydrogen Bubble Interaction

611

R.I. Février 2007

Impact of Volume Viscosity on a Shock/Hydrogen Bubble Interaction

G. Billet,
ONERA 29, av. de la Division Leclerc, 92322 Châtillon Cedex, FRANCE
V. Giovangigli*†,
CMAP-CNRS, Ecole Polytechnique, 91128 Palaiseau Cedex, FRANCE
G. de Gassowski,
BULL, 20, rue Dieumegard, 93406 Saint-Ouen Cedex, FRANCE

Résumé

We investigate the influence of volume viscosity on a planar shock/hydrogen bubble interaction. The numerical model is two dimensional and involve complex chemistry and detailed transport. All transport coefficients are evaluated using algorithms which provide accurate approximations rigourously derived from the kinetic theory of gases. Our numerical results show that volume viscosity has an important impact on the velocity distribution—through vorticity production—and therefore on the flame structure.

1 Introduction

Combustion models used in the computational study of shock/flame interaction, ignition phenomena, or pollutant formation combine complex chemical kinetics with detailed transport phenomena. One of such phenomenon, often neglected in flame models, is volume—or bulk—viscosity. The volume viscosity coefficient appears in the viscous tensor and, thus, in the momentum and energy conservation equations. In an expansion or contraction of the gas mixture, the work done by the pressure modifies immediately the translational energy of the molecules. A certain time-lag is needed, however, for the re-equilibration of translational and internal energy through inelastic collisions and this relaxation phenomenon gives rise to bulk viscosity [12, 25, 30, 40].

Denoting by κ the volume viscosity and η the shear viscosity, theoretical calculations and experimental measurements have shown that the ratio κ/η is of order unity for polyatomic gases. In the framework of the kinetic theory of gases, theoretical calculations have first been performed for special molecular models like rough spheres, smooth loaded spheres, or hard ellipsoids, and, next, for general polyatomic gases and polyatomic gas mixtures, using transport linear systems [12, 25, 18, 40, 48, 54, 56]. On the other hand, from an experimental point of view, sound absorption is the only demonstrated method for measuring volume viscosity and relatively accurate results are available in the literature [33, 40, 45, 46]. These experiments have shown for instance that at room temperature the ratio κ/η is approximately 0.73 for N_2, 33.4 for H_2, 0.55 for CO, 1.30 for NH_3, and 1.33 for CH_4. Note in particular the relatively high value of κ/η for hydrogen which is the fuel under consideration in this paper. Only rotational internal degrees of freedom are active at room temperature for these molecules [18, 40, 54]. Much larger values of the ratio κ/η at room temperature have also been reported for CO_2 and N_2O—associated with degenerated vibrational states—as well as for liquids [53, 36, 15, 16]. As a consequence, the term associated with bulk viscosity in the viscous tensor cannot always be neglected. This is especially the case for a variety of compressible flow applications where the dilatation $\boldsymbol{\nabla}\cdot\boldsymbol{v}$ becomes significant, such as shock/flame interactions, supersonic flames, or hypersonic flows. The effect of volume viscosity on a non similar hypersonic boundary layer has been investigated in particular by Emmanuel [16]. Bulk viscosity has been found to significantly increase wall heat transfers under hypersonic conditions in CO_2 atmospheres [16].

*†Corresponding author. E-mail : vincent.giovangigli@polytechnique.edu

Despite its potential importance, volume or bulk viscosity has seldom been included in computational models of multidimensional reactive flows [15, 16, 30]. The main reasons have been overconfidence in the erroneous Stokes hypothesis, the weak impact of volume viscosity on small Mach number flows [27], the weak impact of volume viscosity on classical boundary layers and the costs associated with the evaluation of volume viscosity in multicomponent mixtures. It is now possible, however, to evaluate multicomponent transport coefficients from rigourous accurate expressions at a moderate computational cost [17, 18, 19, 20, 21].

More generally, recent numerical investigations have brought further support for the importance of accurate transport property in various multicomponent reactive flows. Thermal diffusion effects have been shown to be important in the study of vortex-flame interaction [32], catalytic effects near walls [4], interfacial phenomena [49], gaseous or spray diffusion flames [26, 6], and chemical vapor deposition reactors [24]. The impact of multicomponent diffusion has also been shown to be important in multidimensional hydrogen/air and methane/air Bunsen flames [22], in freely propagating flames—especially with oxygen as pure oxydizer—[23, 5], as well as in direct numerical simulation of turbulent flames [34].

The goal of this paper is to investigate the impact of volume viscosity on a planar air shock/hydrogen bubble interaction. This flow configuration has already been considered by several authors [10, 31, 43, 14, 50, 47]. The propagation of shocks through gas nonuniformities results in refraction, diffraction and reflexion of shock waves at inhomogeneities. The interaction of pressure waves with density fluctuations is then a major source of vorticity. The resulting unsteady reactive flow appears to be a good test case to measure the impact of volume viscosity.

The simulation of severe flow conditions, such as unsteady reactive supersonic flows, requires robust accurate numerical methods. A time splitting method is used with separate finite difference operators for convective terms, dissipative terms—associated with diffusion, thermal conduction, and viscosity—and chemistry sources. The finite difference operator associated with convection is split in each spatial direction and the corresponding algorithm is shock capturing. Around the shock, Godunov algorithm is used whereas away from the shock a third order MUSCL algorithm with triad adaptive limiters is used [9, 10]. The dissipative operator is discretized with second order centered finite differences. The resulting numerical algorithms have been tested intensively on various flow phenomena such as acoustic waves propagation, refraction waves, focusing shock waves, vortex/flame interaction, acoustic wave/flame interaction, mixing layers, Kelvin-Helmholtz instabilities and complex chemistry laminar flames [7, 8, 9, 10].

In the next section we formulate the model used to describe multidimensional flames. In Section 3 we discuss experimental and theoretical evaluations of volume viscosity. In Section 4, we address important issues concerning volume viscosity and fluid mechanics. The numerical method is described in Section 5 and the numerical results are finally presented in Sections 6 and 7.

2 Model formulation

We investigate in this section the model used to analyze the shock/bubble interaction. We present the conservation equations, the transport fluxes, the thermochemistry properties, and discuss the evaluation of transport coefficients.

2.1 Conservation equations

The equations governing multicomponent flows are derived from the kinetic theory of gases and express conservation of species mass, momentum, and energy [57, 27]. These equations may be written in the form

$$\partial_t(\rho Y_i) + \boldsymbol{\nabla}\cdot(\rho \boldsymbol{v} Y_i) + \boldsymbol{\nabla}\cdot(\rho Y_i \boldsymbol{V}_i) = m_i \omega_i, \quad i \in \mathcal{S}, \tag{1}$$

$$\partial_t(\rho \boldsymbol{v}) + \boldsymbol{\nabla}\cdot(\rho \boldsymbol{v}\otimes\boldsymbol{v} + p\boldsymbol{I}) + \boldsymbol{\nabla}\cdot\boldsymbol{\Pi} = 0, \tag{2}$$

$$\partial_t\big(\rho(e + \tfrac{1}{2}\boldsymbol{v}\cdot\boldsymbol{v})\big) + \boldsymbol{\nabla}\cdot\big(\rho(e + \tfrac{1}{2}\boldsymbol{v}\cdot\boldsymbol{v} + p)\big) + \boldsymbol{\nabla}\cdot(\boldsymbol{q} + \boldsymbol{\Pi}\cdot\boldsymbol{v}) = 0, \tag{3}$$

where ∂_t is the time derivative operator, $\boldsymbol{\nabla}$ the space derivative operator, ρ the density, $\boldsymbol{v}$ the mass averaged flow velocity, Y_i the mass fraction of the i^{th} species, $\boldsymbol{V}_i$ the diffusion velocity of the i^{th} species, m_i the molar weight of the i^{th} species, ω_i the molar production rate of the i^{th} species, $\mathcal{S} = \{1, \ldots, n\}$ the species indexing set, n the number of species in the mixture, $\boldsymbol{\Pi}$ the viscous tensor, p the pressure, e the internal energy per unit mass, and $\boldsymbol{q}$ the heat flux vector.

2.2 Thermodynamics

Thermodynamics obtained in the framework of the kinetic theory of gases is valid out of equilibrium and has, therefore, a wider range of validity than classical thermodynamics introduced for stationary homogeneous equilibrium states. The pressure is given by

$$p = \rho \mathrm{R} T \sum_{k \in \mathcal{S}} \frac{Y_k}{m_k}, \tag{4}$$

where T is the absolute temperature and R the gas constant. The internal energy per unit mass e can be written as

$$e = \sum_{k \in \mathcal{S}} Y_k e_k, \tag{5}$$

where e_k is the specific internal energy of the k^{th} species given by

$$e_k = e_k^{\text{std}} + \int_{T^{\text{std}}}^{T} c_{vk}(\tau)\, d\tau, \qquad k \in \mathcal{S}, \tag{6}$$

and where e_k^{std} is the standard formation energy of the k^{th} species at the standard temperature T^{std} and c_{vk} the constant volume specific heat of the k^{th} species. The entropy per unit mass s can be written in the form

$$s = \sum_{k \in \mathcal{S}} Y_k s_k, \tag{7}$$

where s_k is the specific entropy of the k^{th} species given by

$$s_k = s_k^{\text{std}} + \int_{T^{\text{std}}}^{T} \frac{c_{vk}(\tau)}{\tau}\, d\tau - \frac{\mathrm{R}}{m_k} \log\left(\frac{\rho_k}{\gamma^{\text{std}} m_k}\right), \quad k \in \mathcal{S}, \tag{8}$$

and where s_k^{std} is the formation entropy of the k^{th} species at the standard temperature T^{std} and standard pressure $p^{\text{std}} = p^{\text{atm}}$, $\rho_k = Y_k \rho$ the mass density of the k^{th} species, and $\gamma^{\text{std}} = p^{\text{std}}/\mathrm{R}T^{\text{std}}$ is the standard concentration. Similarly, one can introduce the mixture enthalpy per unit mass h and mixture Gibbs function per unit mass g which can be written $h = \sum_{k \in \mathcal{S}} Y_k h_k$, and $g = \sum_{k \in \mathcal{S}} Y_k g_k$, where $h_k = e_k + \mathrm{R}T/m_k$ and $g_k = h_k - T s_k$, $k \in \mathcal{S}$.

2.3 Chemistry

The molar production rates ω_i, $i \in \mathcal{S}$, are of Maxwellian type and are compatible with the law of mass action [27]. We consider a complex reaction mechanism involving an arbitrary number of elementary chemical reactions

$$\sum_{k \in \mathcal{S}} \nu_{ki}^{\mathrm{d}} \mathcal{X}_k \;\rightleftharpoons\; \sum_{k \in \mathcal{S}} \nu_{ki}^{\mathrm{r}} \mathcal{X}_k, \qquad i \in \mathcal{R}, \tag{9}$$

where ν_{ki}^{d} and ν_{ki}^{r} are the direct and reverse stoichiometric coefficients of the k^{th} species in the i^{th} reaction, $\mathcal{R} = \{1, \ldots, n^r\}$ is the reaction indexing set, n^r the number of chemical reactions, and where $\mathcal{X}_k$ is a symbol for the k^{th} species. The Maxwellian rate of production for the k^{th} species, as derived from the kinetic theory of gases, is given by

$$\omega_k = \sum_{i \in \mathcal{R}} \nu_{ki} r_i, \tag{10}$$

where $\nu_{ki} = \nu_{ki}^{\mathrm{r}} - \nu_{ki}^{\mathrm{d}}$ and r_i is the rate of progress of the i^{th} reaction. The rate of progress r_i is the difference between the direct and reverse rates

$$r_i = \mathcal{K}_i^{\mathrm{d}} \prod_{k \in \mathcal{S}} \Big(\frac{\rho_k}{m_k}\Big)^{\nu_{ki}^{\mathrm{d}}} - \mathcal{K}_i^{\mathrm{r}} \prod_{k \in \mathcal{S}} \Big(\frac{\rho_k}{m_k}\Big)^{\nu_{ki}^{\mathrm{r}}}, \tag{11}$$

where ρ_k/m_k is the molar concentration of the k^{th} species and $\mathcal{K}_i^{\mathrm{d}}$ and $\mathcal{K}_i^{\mathrm{r}}$ are the direct and reverse reaction constants for the i^{th} reaction. The reaction constant $\mathcal{K}_i^{\mathrm{d}}$ is usually estimated by an Arrhenius expression whereas $\mathcal{K}_i^{\mathrm{r}}$ is evaluated from the relation $\mathcal{K}_i^{\mathrm{d}}/\mathcal{K}_i^{\mathrm{r}} = \mathcal{K}_i^{\mathrm{e}}$ where $\mathcal{K}_i^{\mathrm{e}}$ is the equilibrium constant of the i^{th} reaction. These reciprocity relations between the direct and reverse reaction constants are direct consequences of reciprocity relations between molecular reactive transition probabilities [27].

2.4 Transport fluxes

In the framework of the kinetic theory of dilute polyatomic gas mixtures, the transport fluxes $\boldsymbol{V}_i$, $i \in \mathcal{S}$, $\boldsymbol{\Pi}$, and $\boldsymbol{q}$, are expressed in terms of transport coefficients and macroscopic variable gradients [12, 25, 57, 56, 27]

$$\rho Y_i \boldsymbol{V}_i = -\sum_{j\in\mathcal{S}} \rho Y_i D_{ij}(\boldsymbol{d}_j + \widetilde{\chi}_j X_j \boldsymbol{\nabla}\log T), \qquad i \in \mathcal{S}, \tag{12}$$

$$\boldsymbol{\Pi} = -\kappa\, \boldsymbol{\nabla}\cdot\boldsymbol{v}\, \boldsymbol{I} - \eta\Big(\boldsymbol{\nabla}\boldsymbol{v} + (\boldsymbol{\nabla}\boldsymbol{v})^t - \tfrac{2}{3}\,\boldsymbol{\nabla}\cdot\boldsymbol{v}\, \boldsymbol{I}\Big), \tag{13}$$

$$\boldsymbol{q} = \sum_{i\in\mathcal{S}} \rho h_i Y_i \boldsymbol{V}_i - \lambda\boldsymbol{\nabla}T + \mathrm{R}T\sum_{i\in\mathcal{S}} \widetilde{\chi}_i \frac{\rho Y_i \boldsymbol{V}_i}{m_i}, \tag{14}$$

where D_{ij}, $i,j \in \mathcal{S}$, are the multicomponent diffusion coefficients, $\boldsymbol{d}_i$, $i \in \mathcal{S}$, the species diffusion driving forces, $\widetilde{\chi}_i$, $i \in \mathcal{S}$, the rescaled thermal diffusion ratios, X_i, $i \in \mathcal{S}$, the species mole fractions, κ the bulk viscosity, η the shear viscosity, $\boldsymbol{I}$ the unit tensor, h_i the enthalpy per unit mass of the i^{th} species, and λ the thermal conductivity. The diffusion driving force $\boldsymbol{d}_i$ for the i^{th} species is given by

$$\boldsymbol{d}_i = \boldsymbol{\nabla}X_i + (X_i - Y_i)\boldsymbol{\nabla}\log p, \qquad i \in \mathcal{S}. \tag{15}$$

The transport coefficients introduced in the definition of the transport fluxes (12)–(14) have important properties. The diffusion matrix is symmetric, i.e., $D_{ij} = D_{ji}$ for $i,j \in \mathcal{S}$ and we have $\sum_{i\in\mathcal{S}} Y_i D_{ij} = 0$ for $j \in \mathcal{S}$. Symmetric diffusion matrices have been introduced by Waldmann [56] and considered by Chapmann and Cowling [12] and Ferziger and Kaper [25] and are compatible with Onsager's reciprocity relations. The property $\sum_{i\in\mathcal{S}} Y_i D_{ij} = 0$, $j \in \mathcal{S}$, yields the important mass conservation constraint for the species diffusion velocities

$$\sum_{i\in\mathcal{S}} Y_i \boldsymbol{V}_i = 0. \tag{16}$$

In addition, the matrix D is positive definite on the hyperplane of zero-sum driving forces and we have $\eta > 0$, $\lambda > 0$, and $\kappa \geq 0$. These properties are consequences of the kinetic theory of gases and yield positivity of entropy production due to macroscopic variable gradients [12, 25, 17, 56].

2.5 Transport coefficients

The transport coefficients needed to express the transport fluxes are functions of the state of the mixture, i.e., of pressure, temperature, and species mass fractions. However, the kinetic theory of gases does not yield explicit expressions for the mixture transport coefficients but instead linear systems which must be solved first [12, 25, 17, 56, 57]. The general mathematical structure of these systems has been obtained in [17] under very general assumptions. In particular, it was shown in [17, 19] that the transport coefficients can be expanded as convergent series, thus yielding rigorous approximate expressions by truncation. In addition, various new linear systems and approximate expressions have been obtained for all the mixture transport coefficients. Optimized transport algorithms for flame modeling have then been derived and investigated numerically on several computer architectures [19, 20]. Large speedups have been measured on various machines with respect to other existing software. These algorithms are included in a Fortran library available for academic purposes [21].

3 Volume viscosity and relaxation

We discuss in this section experimental measurements as well as theoretical issues about volume viscosity in dilute gases.

3.1 Attenuation of acoustic waves

Acoustic absorption measurement of a sound wave is the only demonstrated method capable of estimating bulk viscosity [15, 16, 33, 36, 30, 40, 45, 46]. For a single polyatomic gas, one can establish that, in the low frequency and small attenuation limits, the spatial sound absorption coefficient α is given by [33, 46]

$$\frac{\alpha}{\omega^2} = \frac{2\pi^2}{\rho c^3}\Big(\tfrac{4}{3}\eta + \kappa + \frac{c_p - c_v}{c_p c_v}\lambda\Big), \tag{17}$$

where ω is the sound wave frequency, c the sound velocity, c_p the specific heat at constant pressure, and c_v the specific heat at constant volume of the gas under consideration. This formula is valid when $\omega\tau \ll 1$ where τ denotes the particle collision time or any relaxation time for internal energy of the gas molecules. From an experimental point of view, a condensor-type sound transducer transmits plane sound waves at a steady rate. The waves are detected with a condensor microphone which moves away at a constant speed. The detected signal is fed into a selective amplifier and plotted on a logarithmic level recorder. The absorption coefficient α is then determined as the slope of the experimental plot.

Numerous experiments have been performed in the seventies, in particular by the group of Professor J.J.M. Beenakker [33, 45, 46]. The ratios κ/η at room temperature evaluated from these measurements are presented in Table 3.1 for various gases. All these experimental values are at least of order $O(1)$ and we have in particular $\kappa/\eta = 0.73$ for N_2, $\kappa/\eta = 1.33$ for CH_4, and a relatively large value $\kappa/\eta = 33.4$ for H_2 which is the fuel under consideration in this paper. Even if the method involves potential error, because one measures a total absorption coefficient α and then substracts the contributions to absorption due to shear viscosity η and thermal conduction λ, the experimental errors are estimated to be below 10% [33, 45, 46]. These measurements clearly indicate that the ratio κ/η is at least of order unity for polyatomic gases. On the other hand, measurements performed for Ne, which is a monatomic gas, have confirmed that the corresponding volume viscosity is zero [46]. Nevertheless, since bulk viscosity also arise in dense gases and in liquids, its absence in dilute monatomic gases is an exception rather a rule [25, 30].

Evaluation of the ratio κ/η at room temperature from experimental measurements [33, 45, 46].

Gas	N_2	H_2	D_2	CO	NH_3	CH_4	CD_4
κ/η	0.73	33.4	20.6	0.55	1.30	1.33	1.17

Note that only rotational mode is active for these gases at room temperature [18, 33, 45, 46, 40]. On the other hand, much larger values of the ratio κ/η have been reported by Tisza for CO_2 and N_2O molecules, which have degenerated vibrational states [15, 16, 30, 53]. However, large values of the vibrational volume viscosity, that is, large values of vibrational relaxation times at room temperature, can only be described by using vibrational desequilibrium models with several temperatures [30]. These models, which are not relevant for standard combustion applications, should still take into account a rotational volume viscosity if translational and rotational temperatures are at partial thermodynamic equilibrium.

On the other hand, the expression (17) can be generalized for multicomponent mixtures in the form

$$\frac{\alpha}{\omega^2} = \frac{2\pi^2}{\rho c^3}\Big(\tfrac{4}{3}\eta + \kappa + \frac{c_p - c_v}{c_p c_v}\lambda + \frac{c_p}{c_v}\sum_{k,l\in\mathcal{S}} \rho D_{kl}(X_k + \frac{r}{c_p}\chi_k)(X_l + \frac{r}{c_p}\chi_l)\Big), \tag{18}$$

where X_k is the mass fraction of the k^{th} species and $\chi_k = X_k\widetilde{\chi}_k$ the Waldmann coefficients of the k^{th} species, related to Soret and Dufour effects. Therefore, in mixtures, there exists a contribution to absorption due to multicomponent diffusion in the form

$$\frac{c_p}{c_v}\sum_{k,l\in\mathcal{S}} \rho D_{kl}(X_k + \frac{r}{c_p}\chi_k)(X_l + \frac{r}{c_p}\chi_l). \tag{19}$$

This formula (19) can be shown to coincide with the result of Hirschfelder, Curtiss and Bird [35], but has a *much simpler* analytic expression, thanks to the use of the Waldmann coefficients and to the natural symmetry of the diffusion matrix D that has been artificially destroyed in [35]. Furthermore, this quantity (19) is obviously nonnegative because the diffusion matrix $D = (D_{ij})_{i,j\in\mathcal{S}}$ is positive semidefinite. Since the nullspace of D is also spanned by the mass fraction vector $Y = (Y_1, \ldots, Y_n)^t$ [27] the contribution of multicomponent diffusion to absorption (19) is zero if and only if $X_k + \frac{r}{c_p}\chi_k = Y_k$ for $k \in \mathcal{S}$.

3.2 Relaxation of internal energy

In a gas with internal energy degrees of freedom, the energy partition between the translational and internal degrees of freedom in non-equilibrium need not be the same as in equilibrium. If a small element of gas is suddenly compressed, the energy deposited in the gas initially becomes energy associated with the translational motion and only later do the internal degrees of freedom receive any of it. Since the

pressure arises entirely from the translational motion of molecules, it will be somewhat higher initially than it would be if equilibrium between the translational and internal degrees of freedom would be instantaneously established. Thus the effect is equivalent to having an enhanced hydrostatic pressure in a compressed gas, for which $\boldsymbol{\nabla}\cdot\boldsymbol{v} < 0$, and a reduced hydrostatic pressure in an expanded gas for which $\boldsymbol{\nabla}\cdot\boldsymbol{v} > 0$.

Consider, for the sake of simplicity, a pure polyatomic gas with a single internal energy mode close to equilibrium. By using a moment method—and neglecting second order effects—one can establish relaxation equations typically in the form [12, 25, 40]

$$\partial_t T^{\rm int} + \boldsymbol{v}\cdot T^{\rm int} = -\frac{T^{\rm tr} - T^{\rm int}}{\tau^{\rm int}}, \tag{20}$$

where $T^{\rm tr}$ is the translational temperature, $T^{\rm int}$ the internal temperature, and $\tau^{\rm int}$ the internal energy relaxation time. The energy per unit mass of the gas is given by $c_v T = c^{\rm tr}T^{\rm tr} + c^{\rm int}T^{\rm int}$ so that we also have $c_v(T^{\rm tr} - T) = c^{\rm int}(T^{\rm tr} - T^{\rm int})$. In particular, assuming that $T^{\rm tr}$ is constant, then $T^{\rm int}$ and T converge exponentially towards $T^{\rm tr}$ with the characteristic time $\tau^{\rm int}$. The relaxation time $\tau^{\rm int}$ is then related to the volume viscosity κ with

$$\kappa = \frac{pR}{c_v^2} c^{\rm int}\tau^{\rm int}, \tag{21}$$

where $c^{\rm int}$ is the internal heat capacity [12, 25, 40]. At first order in the Enskog expansion, the temperature differences can be shown to be [12, 25, 40]

$$T^{\rm tr} - T = -\frac{c^{\rm int}R}{c_v^2} T\tau^{\rm int}\,\boldsymbol{\nabla}\cdot\boldsymbol{v}. \tag{22}$$

3.3 Transport linear systems for κ

When there are several modes for internal energy and/or several species present in the mixture, the simple relation (21) is replaced by the solution of a transport linear system providing the volume viscosity. The species characteristic times for relaxation of internal energy as well as collision integrals then appear as parameters in the coefficients of the transport linear system. The transport linear system also depends on the orthogonal polynomial expansions used to represent the perturbed distribution function associated with volume viscosity [17, 18, 40, 48, 54].

The traditional transport linear system associated with volume viscosity is of size $n+n^p$, where n^p is the number of polyatomic species. The corresponding system coefficients are given in a non symmetric form in [48]—with a misprint identified in [17]—and are given in their natural symmetric form in [17, 18]. Several numerical applications associated with combustion are also presented in [17, 18]. A simplified system of size n^p has also been obtained by reducing the variational approximation space used to develop the perturbed distribution functions associated with volume viscosity [17]. Within the Monchick and Mason approximations, neglecting complex collisions with more than one quantum jump, the reduced system is diagonal and typically yields

$$\kappa = \frac{pR}{c_v^2} \sum_{k\in\mathcal{P}} X_k c_k^{\rm int}\tau_k^{\rm int}, \tag{23}$$

where $\mathcal{P} = \{1, \ldots, n^p\}$ is the polyatomic species indexing set, and where the average relaxation time for internal energy of the $k^{\rm th}$ species $\tau_k^{\rm int}$ is given by

$$\frac{c_k^{\rm int}}{\tau_k^{\rm int}} = \sum_{{\rm m}\in\mathcal{M}} \frac{c_k^{\rm m}}{\tau_k^{\rm m}}, \tag{24}$$

where $\tau_k^{\rm m}$ is the average relaxation time of internal energy in mode m for the $k^{\rm th}$ species, and $\mathcal{M}$ is the internal energy mode indexing set. Note that harmonic means are obtained for relaxation times when polynomials in the total energy are considered in the expansions of the species perturbed distribution functions [17, 18]. This expression of $\tau_k^{\rm int}$ yields a natural transition between frozen and active modes when temperature is varying. On the other hand, when polynomials in each energy modes are considered, arithmetic means are obtained between the modes [12, 18]

$$c_k^{\rm int}\tau_k^{\rm int} = \sum_{{\rm m}\in\mathcal{M}} c_k^{\rm m}\tau_k^{\rm m}. \tag{25}$$

4 Volume viscosity and fluid mechanics

The preceding sections have shown that Stokes hypothesis is *erroneous* in the sense that the ratio κ/η is always of order unity or larger for polyatomic gases which are generally the gases of practical interest. Even more, volume viscosity also arises in dense gases and in liquids, and its absence in dilute monatomic gases is an exception rather than a rule [25, 30]. Still, it is taken for granted in most expositions of fluid dynamics that $\kappa/\eta << 1$ and justification for this—erroneous—belief is elusive. Since fluid mechanics has been quite successful in the past we have to explain this paradox or apparent contradiction. To this aim, we discuss in this section a number of situations where the whole term $\boldsymbol{\nabla}\cdot(\kappa\boldsymbol{\nabla}\cdot\boldsymbol{v}\,\boldsymbol{I})$ has a small influence, because of its *structure*, even though both the ratio κ/η and the dilatation $\boldsymbol{\nabla}\cdot\boldsymbol{v}$ are not small. We also discuss the impact of the volume viscosity κ on weak shocks internal structure.

4.1 Volume viscosity and small Mach number flows

Let us consider the equations governing a fluid in the small Mach number limit. In this situation, we classically have the pressure decomposition $p = p_{\rm u} + \widetilde{p}$ where $p_{\rm u}$ is spatially uniform and $\widetilde{p}$ is the fluid dynamic perturbation with $\widetilde{p}/p_{\rm u} = O({\rm Ma}^2)$, where Ma is the Mach number. This pressure decomposition yields the simplified momentum equation

$$\partial_t(\rho\boldsymbol{v}) + \boldsymbol{\nabla}\cdot(\rho\boldsymbol{v}\otimes\boldsymbol{v} + \widetilde{p}\boldsymbol{I}) - \boldsymbol{\nabla}\cdot\Big(\kappa\,\boldsymbol{\nabla}\cdot\boldsymbol{v}\,\boldsymbol{I} + \eta\big(\,\boldsymbol{\nabla}\boldsymbol{v} + (\boldsymbol{\nabla}\boldsymbol{v})^t - \tfrac{2}{3}\,\boldsymbol{\nabla}\cdot\boldsymbol{v}\,\boldsymbol{I}\,\big)\Big) = 0. \tag{26}$$

However, introducing the new perturbed pressure $\widehat{p}$ defined by

$$\widehat{p} = \widetilde{p} - \kappa\boldsymbol{\nabla}\cdot\boldsymbol{v}, \tag{27}$$

the momentum equation (26) can be recast in the form

$$\partial_t(\rho\boldsymbol{v}) + \boldsymbol{\nabla}\cdot(\rho\boldsymbol{v}\otimes\boldsymbol{v} + \widehat{p}\boldsymbol{I}) + \boldsymbol{\nabla}\cdot\Big(\eta\big(\,\boldsymbol{\nabla}\boldsymbol{v} + (\boldsymbol{\nabla}\boldsymbol{v})^t - \tfrac{2}{3}\boldsymbol{\nabla}\cdot\boldsymbol{v}\boldsymbol{I}\,\big)\Big) = 0. \tag{28}$$

We observe then that the boundary conditions associated with both perturbed pressures $\widetilde{p}$ and $\widehat{p}$ are often identical. Assuming that this is indeed the case, the volume viscosity term $\boldsymbol{\nabla}\cdot(\kappa\boldsymbol{\nabla}\cdot\boldsymbol{v}\,\boldsymbol{I})$ is then exactly absorbed in the perturbed pressure term, so that temperature, velocity and species mass fractions are *strictly* unchanged by volume viscosity. Note that the divergence of the velocity field may be large in small Mach number flows, as for instance in a flame front, where large temperature variations induce large density variations, and, consequently, large variations in $\boldsymbol{\nabla}\cdot\boldsymbol{v}$. In this situation, both κ and $\boldsymbol{\nabla}\cdot\boldsymbol{v}$ are large, but since they only appear in the form of a gradient $\boldsymbol{\nabla}\cdot(\kappa\boldsymbol{\nabla}\cdot\boldsymbol{v}\,\boldsymbol{I}) = \boldsymbol{\nabla}(\kappa\boldsymbol{\nabla}\cdot\boldsymbol{v})$, the group $\kappa\boldsymbol{\nabla}\cdot\boldsymbol{v}$ only modifies the perturbed pressure.

More generally, in such a situation, using a fully compressible formulation instead of a small Mach number model, the temperature, velocity and species mass fractions will only be modified by $O({\rm Ma}^2)$ quantities when neglecting the volume viscosity term.

Therefore, the term that can be considered to be negligible in the small Mach number limit is the complete group $\boldsymbol{\nabla}\cdot(\kappa\boldsymbol{\nabla}\cdot\boldsymbol{v}\,\boldsymbol{I})$. This term can be neglected because of its structure, even though both the ratio κ/η and the dilatation $\boldsymbol{\nabla}\cdot\boldsymbol{v}$ may not be small, as was already mentioned in [27]. We could even consider the conservation equation

$$\partial_t(\rho\boldsymbol{v}) + \boldsymbol{\nabla}\cdot(\rho\boldsymbol{v}\otimes\boldsymbol{v} + \overline{p}\boldsymbol{I}) + \boldsymbol{\nabla}\cdot\Big(\eta\big(\boldsymbol{\nabla}\boldsymbol{v} + (\boldsymbol{\nabla}\boldsymbol{v})^t\big)\Big) = 0. \tag{29}$$

with $\overline{p} = \widetilde{p} - (\kappa - \frac{2}{3}\eta)\boldsymbol{\nabla}\cdot\boldsymbol{v}$, and here again the boundary conditions associated with $\widetilde{p}$, $\widehat{p}$, or $\overline{p}$ are often similar. In this situation, the whole group $\boldsymbol{\nabla}\cdot\big((\kappa - \frac{2}{3}\eta)\boldsymbol{\nabla}\cdot\boldsymbol{v}\,\boldsymbol{I}\big)$ can be absorbed in the perturbed pressure.

Further note that, in the small Mach number limit, the density ρ is given by the simplified state law $\rho = p_{\rm u}/RT\sum_{k\in\mathcal{S}}\frac{Y_k}{m_k}$ and only depends on T and on the species mass fractions. As a consequence, the total mass conservation equation yields a constraint on the divergence of the velocity fields $\boldsymbol{\nabla}\cdot\boldsymbol{v}$. This constraint can only be satisfied through the presence of a gradient in the momentum equation—as for incompressible flows— so that the perturbed pressure gradient can be interpreted as a Lagrange multiplier.

4.2 Normal boundary layers

There are at least two other situations where volume viscosity has a small influence. These are high Reynolds number flows and classical boundary layer flows. This is quite straightforward for high Reynolds number flows since dissipative effects are then much smaller than inertial effects. On the other hand, volume viscosity turns out to be absent from classical second order boundary layer equations. Indeed, the tangential momentum equation in a boundary layer is typically in the form

$$\rho v_\tau \partial_\tau v_\tau + \rho v_n \partial_n v_\tau + \partial_\tau p - \partial_n(\eta \partial_n v_\tau) = 0,$$

where τ denotes a tangential coordinate, n a normal coordinate, v_τ and v_n the tangential and normal velocity components. The normal momentum equation is also typically in the form $\partial_n p = 0$. As a consequence, the coefficient κ is absent from second order boundary layers equations and only appears in *third order* models [16]. This again shows that the group $\boldsymbol{\nabla}\cdot(\kappa\boldsymbol{\nabla}\cdot\boldsymbol{v}\,\boldsymbol{I})$ has little or no influence on these flows because of its structure, even if the ratio κ/η and the dilatation $\boldsymbol{\nabla}\cdot\boldsymbol{v}$ are not small.

On the other hand, Emmanuel has investigated hypersonic boundary layer flows with very large values of the volume viscosity κ corresponding to CO_2 atmospheres. Thanks to the large value of the corresponding ratio $\kappa/\eta \simeq 2000$ for CO_2, Emmanuel has introduced a scaling that promotes the volume viscosity term from third to second order. In this situation, volume viscosity terms have been shown to significantly change wall heat tranfers [16].

4.3 Shock internal structure

The internal structure of weak shocks waves has been investigated by several authors [38, 51]. For weak shock, the Navier–Stokes equations are fully valid inside the shock. One can then either solve the full Navier–Stokes equations numerically or use asymptotic techniques to investigate the internal shock structure. Taylor asymptotic analysis yields the pressure profile inside weak shocks as function of the upstream and downtream states and involves the same combination of transport coefficients $\frac{4}{3}\eta + \kappa + \frac{c_p - c_v}{c_p c_v}\lambda$ as for sound absorption [13, 38, 52, 51]. More specifically, the asymptotic internal shock pressure profile is found in the form

$$p = \frac{p_2 + p_1}{2} + \frac{p_2 - p_1}{2}\,\tanh(\frac{x}{\delta}) \tag{30}$$

where p_1 is the upstream pressure, p_2 the downstream pressure, x the cartesian coordinate normal to the planar shock, and δ the internal shock characteristic length. The length δ is given by [13, 38, 51]

$$\delta = \frac{4}{\gamma+1}\frac{1}{\rho(v_1 - v_2)}\Big(\tfrac{4}{3}\eta + \kappa + \frac{c_p - c_v}{c_p c_v}\lambda\Big), \tag{31}$$

where $\gamma = c_p/c_v$ is the ratio of specific heats, $v_1 = v(-\infty)$ the upstream velocity, $v_2 = v(+\infty)$ the downstream velocity, and all the thermodynamic and transport coefficients are taken to be constant in these simplified asymptotic models. This formula (31) still shows that, in the presence of volume viscosity, the thickness of shock waves is larger.

Experiments and numerical simulations have shown that the results obtained in the framework of weak shocks are indeed valid for stronger shocks. More specifically, integrating the Navier-Stokes equations with temperature dependent thermodynamic and transport coefficients yields reasonably accurate results up to shocks with Ma = 2 [3, 42, 51]. Hence we expect shock waves to be much thicker in hydrogen during the shock-bubble interaction since the corresponding ratio κ/η is much larger than unity. Nevertheless, these theories strictly concern one dimensional steady shocks. In a multidimensional, unsteady, reactive situation, these simplified one dimensional models are not completely valid, and we can only expect a qualitative agreement.

For strong shocks the Navier-Stokes equations fail and cannot be used to describe the internal shock structure [3, 29, 37]. Nevertheless, accurate description of the internal shock structure have been obtained by using the Navier-Stokes entropy production formula together with linear internal profiles [37]. Since entropy production reads

$$\lambda\frac{|\boldsymbol{\nabla}T|^2}{T^2} + \frac{\eta}{2T}\big(\boldsymbol{\nabla}\boldsymbol{v} + (\boldsymbol{\nabla}\boldsymbol{v})^t - \tfrac{2}{3}\boldsymbol{\nabla}\cdot\boldsymbol{v}\,\boldsymbol{I}\big):\big(\boldsymbol{\nabla}\boldsymbol{v} + (\boldsymbol{\nabla}\boldsymbol{v})^t - \tfrac{2}{3}\boldsymbol{\nabla}\cdot\boldsymbol{v}\,\boldsymbol{I}\big) + \kappa\frac{|\boldsymbol{\nabla}\cdot\boldsymbol{v}|^2}{T},$$

we still expect an impact of the volume viscosity κ on the corresponding internal shock structures.

4.4 Vorticity equation

For convenience, we discuss in this section the vorticity equation since vorticity $\zeta = \boldsymbol{\nabla} \wedge \boldsymbol{v}$ is at the origin of the flow complexities during the shock-bubble interaction. The vorticity equation reads

$$\partial_t \zeta + \boldsymbol{v}\cdot\boldsymbol{\nabla}\zeta = \zeta\cdot\boldsymbol{\nabla}\boldsymbol{v} - \zeta\boldsymbol{\nabla}\cdot\boldsymbol{v} + \tfrac{1}{\rho^2}\boldsymbol{\nabla}\rho \wedge \boldsymbol{\nabla}p - \tfrac{1}{\rho^2}\boldsymbol{\nabla}\rho \wedge \boldsymbol{\nabla}\big(\kappa\boldsymbol{\nabla}\cdot\boldsymbol{v}\big) + \boldsymbol{\nabla} \wedge \Big(\tfrac{1}{\rho}\boldsymbol{\nabla}\cdot\big(\eta(\boldsymbol{\nabla}\boldsymbol{v} + (\boldsymbol{\nabla}\boldsymbol{v})^t - \tfrac{2}{3}\boldsymbol{\nabla}\cdot\boldsymbol{v}\boldsymbol{I})\big)\Big). \tag{32}$$

On the right hand side, the first source term $\zeta\cdot\boldsymbol{\nabla}\boldsymbol{v}$ represents the vorticity production due to stretching or tilting of vortex filaments. The second term $\zeta\boldsymbol{\nabla}\cdot\boldsymbol{v}$ corresponds to an amplification or a decrease of the vorticity according to the sign of $\boldsymbol{\nabla}\cdot\boldsymbol{v}$. The third term $\frac{1}{\rho^2}\boldsymbol{\nabla}\rho \wedge \boldsymbol{\nabla}p$ is the baroclinic effect and is the most important production term during the shock/bubble interaction. The fourth and fifth terms $-\frac{1}{\rho^2}\boldsymbol{\nabla}\rho\wedge\boldsymbol{\nabla}\big(\kappa\boldsymbol{\nabla}\cdot\boldsymbol{v}\big)$ and $\boldsymbol{\nabla}\wedge\big(\frac{1}{\rho}\boldsymbol{\nabla}\cdot(\eta(\boldsymbol{\nabla}\boldsymbol{v}+(\boldsymbol{\nabla}\boldsymbol{v})^t-\frac{2}{3}\boldsymbol{\nabla}\cdot\boldsymbol{v}\boldsymbol{I}))\big)$ indicate how volume and shear viscosities create or destroy vorticity.

5 Numerical algorithms

5.1 Splitting of finite difference operators

The simulation of severe flow conditions, such as unsteady reactive supersonic flows, requires robust accurate numerical methods. We use an operator splitting technique with separate operators for convective terms, dissipative terms, and chemistry sources. The splitting can be written in the symbolic form

$$\mathcal{L}_{H_x}(\delta t)\,\mathcal{L}_{H_y}(\delta t)\,\mathcal{L}_P(\delta t)\,\mathcal{L}_S(2\delta t)\,\mathcal{L}_P(\delta t)\,\mathcal{L}_{H_y}(\delta t)\,\mathcal{L}_{H_x}(\delta t)$$

where $\mathcal{L}_{H_x}$ and $\mathcal{L}_{H_y}$ are the finite difference hyperbolic operators in the x and y directions, $\mathcal{L}_P$ the finite difference parabolic operator, $\mathcal{L}_S$ the source operator, and δt the physical time step. The hyperbolic operators $\mathcal{L}_{H_x}$ and $\mathcal{L}_{H_y}$ are shock capturing. Around the shock, Godunov algorithm is used whereas away from the shock a third order MUSCL algorithm with triad adaptive limiters is used [10]. The parabolic operator $\mathcal{L}_P$, which takes into account diffusion, thermal conduction and viscous effects, indeed all dissipative effects, uses second order centered finite differences. The resulting numerical algorithms have been tested intensively on various flow phenomena as such as acoustic waves propagation, refraction waves, focusing shock waves, vortex flame interaction, acoustic wave/flame interaction, mixing layers, Kelvin-Helmholtz instabilities, and complex chemistry laminar flames [7, 8, 9, 10, 11] .

The hyperbolic terms of the Navier-Stokes equations are generally the most difficult to take into account because of the presence of strong nonlinear phenomena in the flow. For these convective terms, adaptive limiters introduced in a MUSCL procedure [55] have been proposed in [1, 7, 8, 9, 10]. Their compressive properties suitably balance the diffusive effects of the flux splitting, such as the AUSM$^+$ splitting [39], and allow to obtain solutions nearly free of numerical instabilities while minimizing numerical dissipation. A simple model called "double flux model" preserving the pressure and the velocity across contact discontinuities has been introduced in [2]. It has been extended to reactive flows composed of species whose constant pressure heat capacities c_{pk}, $k \in \mathcal{S}$, depend on temperature [9]. This extension is taken into account in the hyperbolic operators $\mathcal{L}_{H_x}$ and $\mathcal{L}_{H_y}$.

The resulting set of explicit algorithms, centered-uncentered for the hyperbolic part and centered for the parabolic part, is introduced in a one step scheme [10]. It has the advantage of reducing the number of elementary operations and consequently to produce a cutting down of computational costs while reaching third-order in space and second-order in time accuracies away from the shock. It gives results as accurate as various high order methods like ENO, MENO, WENO, Hermitian, pseudospectral, ACM with wavelet filter schemes, sixth-order centered explicit schemes with fourth-order Runge-Kutta algorithm, and Discontinuous Galerkin [1, 7, 8, 9, 10, 11].

For boundary conditions, the inflow boundary is supersonic whereas the top and bottom boundaries are symmetry boundaries. At the subsonic outflow boundary, characteristic NSCBC boundary conditions are used [44].

5.2 Evaluation of transport coefficients

Highly optimized thermochemistry routines are used in order to evaluate chemical production rates, thermodynamic properties and transport coefficients [19, 20, 21, 28]. While the computational cost of

a direct solve for a transport linear system of size m scales as a multiple of m^3 operations, the computational cost of an iterative method scales as m^2 operations per step. These iterative algorithms only perform one to three iterative steps and are thus more cost-effective than direct inversions in general. The resulting relative errors with respect to a direct linear system solve typically range from 0.1% to 1%. More accurate expressions would not be appropriate since the transport linear systems have been derived by retaining only a few terms in the polynomial expansions of species perturbed distribution functions. The following routines of the eglib library [21] have been used during the calculation : EGFK3 to evaluate the volume viscosity κ, EGFE3 to evaluate the shear viscosity η, EGFYV to evaluate the diffusion velocities from Stefan-Maxwell equations, and EGFLCT1 or EGFLCT3 to evaluate the thermal conductivity λ and the rescaled thermal diffusion ratios $\widetilde{\chi}_k$, $k \in \mathcal{S}$.

6 Planar shock/hydrogen bubble interaction

In this section we investigate numerically the interaction between a planar air shock and a hydrogen bubble. This flow configuration has already been considered by several authors mostly using Euler equations [31, 43, 14, 50, 47, 10] and appears to be a good test case to measure the impact of volume viscosity. From Section 4.1, we indeed know that it is preferable to consider fast flows in order to investigate such an effect.

6.1 Flame characteristics

A two dimensional flow consisting of a planar shock interacting with a hydrogen bubble is considered. The circular bubble—or cylinder—of hydrogen is surrounded by air, moves downstream, and interacts with a steady planar shock initially located at $x = 7$ mm. The schematic of the initial flow configuration is depicted in Figure 1.

Ahead of the shock, the temperature is $T = 1000$ K, the pressure $p = 1$ atm, the Mach number in air $Ma = 2$, the horizontal velocity $v_x = 1240$ m/s, the vertical velocity $v_y = 0$ m/s, and there is only air around the circular bubble. The initial hydrogen bubble has a radius $r = 2.8$ mm and its interface is ≈ 0.25 mm thick. The initial bubble interface is defined by $2Y_{H_2} = 1 + \tanh\big((r_c - r)/C\big)$ where $r^2 = (x - x_0)^2 + (y - y_0)^2$, x, y and r are in mm, $C = 3\ 10^{-2}$, $r_c = 2.8$ mm and $(x_0, y_0) = (4, 0)$ in mm. The interface thickness and the stabilizing effect of diffusion suppress various interface instabilities like Richtmyer-Meshkov or Rayleigh-Taylor [14, 43]. The uniform state downstream of the shock—where there is only air—is calculated from the Rankine-Hugoniot relations. More specifically, Newton's method is used to solve the Rankine-Hugoniot relations, taking into account a variable specific heats ratio $\gamma = c_p/c_v$. The temperature is $T \simeq 1557$ K, the pressure $p \simeq 4.5$ atm, the Mach number $Ma \simeq 0.4$, the horizontal velocity $v_x \simeq 450$ m/s, and the vertical velocity $v_y = 0$ m/s. The time is set to $t = 0$ when the bubble starts to interact with the shock at $x = 7$ mm.

By symmetry, only the upper part of the domain is needed, and the computational domain is taken to be $[0, 30]\times[0, 7.5]$ in mm. The mesh size is $\Delta x = \Delta y = 0.025$ mm so that there are $1201*301$ equispaced grid points. Symmetric boundary conditions are applied at the bottom $y = 0$ mm and at the top $y = 7.5$ mm. Supersonic inflow boundary conditions are applied at the inflow $x = 0$ mm and NSCBC boundary conditions at the subsonic outflow $x = 30$ mm. The time step δt is driven by chemical reactions since we limit the absolute variation of some chemical species, especially HO_2 and H_2O_2, and we typically have $10^{-11} \leq \delta t \leq 5\ 10^{-10}$ where δt is expressed in seconds. The Reynolds number associated with the main vortex is $Re \approx 2800$, the Damköhler number is typically in the range $0.1 \leq Da \leq 10000$, and the Kolmogorov scale is about $\Delta x/10$.

The combustion chemistry of hydrogen in air is taken as in Table 2. The chemical reaction mechanism for H_2–Air includes the $n = 9$ species H_2, O_2, H_2O, H_2O_2, HO_2, OH, H, O, N_2, involved into $n^r = 19$ elementary reactions [41].

The numerical results are presented in Figures 2 to 7 and are discussed in the following sections. Due to file size limitations, the quantities are plotted with a skip of two in the mesh in each direction, excepted for Figs. 6(c) and 6(d), and this postprocessing causes a weak spread of the waves.

Hydrogen-Air Reaction Mechanism [41].
Coefficients in the form $\mathcal{K}_i^{\mathrm{d}} = \mathfrak{A}_i T^{\mathfrak{b}_i} \exp(-\mathfrak{E}_i/RT)$.

i	Reaction	$\mathfrak{A}_i$	$\mathfrak{b}_i$	$\mathfrak{E}_i$
1.	$H_2 + O_2 \rightleftharpoons 2OH$	1.70E+13	0.00	47780.
2.	$OH + H_2 \rightleftharpoons H_2O + H$	1.17E+09	1.30	3626.
3.	$H + O_2 \rightleftharpoons OH + O$	5.13E+16	-0.816	16507.
4.	$O + H_2 \rightleftharpoons OH + H$	1.80E+10	1.00	8826.
5.	$H + O_2 + M \rightleftharpoons HO_2 + M^a$	2.10E+18	-1.00	0.
6.	$H + O_2 + O_2 \rightleftharpoons HO_2 + O_2$	6.70E+19	-1.42	0.
7.	$H + O_2 + N_2 \rightleftharpoons HO_2 + N_2$	6.70E+19	-1.42	0.
8.	$OH + HO_2 \rightleftharpoons H_2O + O_2$	5.00E+13	0.00	1000.
9.	$H + HO_2 \rightleftharpoons 2OH$	2.50E+14	0.00	1900.
10.	$O + HO_2 \rightleftharpoons O_2 + OH$	4.80E+13	0.00	1000.
11.	$2OH \rightleftharpoons O + H_2O$	6.00E+08	1.30	0.
12.	$H_2 + M \rightleftharpoons H + H + M^b$	2.23E+12	0.50	92600.
13.	$O_2 + M \rightleftharpoons O + O + M$	1.85E+11	0.50	95560.
14.	$H + OH + M \rightleftharpoons H_2O + M^c$	7.50E+23	-2.60	0.
15.	$H + HO_2 \rightleftharpoons H_2 + O_2$	2.50E+13	0.00	700.
16.	$HO_2 + HO_2 \rightleftharpoons H_2O_2 + O_2$	2.00E+12	0.00	0.
17.	$H_2O_2 + M \rightleftharpoons OH + OH + M$	1.30E+17	0.00	45500.
18.	$H_2O_2 + H \rightleftharpoons HO_2 + H_2$	1.60E+12	0.00	3800.
19.	$H_2O_2 + OH \rightleftharpoons H_2O + HO_2$	1.00E+13	0.00	1800.

Units are moles, centimeters, seconds, Kelvins, and calories.
[a]Third-body efficiencies : $\alpha_{H_2O} = 21$, $\alpha_{H_2} = 3.3$, $\alpha_{N_2} = 0$, $\alpha_{O_2} = 0$.
[b]Third-body efficiencies : $\alpha_{H_2O} = 6$, $\alpha_{H} = 2$, $\alpha_{H_2} = 3$.
[c]Third-body efficiencies : $\alpha_{H_2O} = 20$.

6.2 Pressure and hydrogen mass fraction

Figures 2 and 3 present isopressure contours and hydrogen mass fraction isopleths at various times. Going from left to right and top to bottom, Figures 2(a) to 2(f) correspond to $t = 1.5$ μs, $t = 2.0$ μs, $t = 2.5$ μs, $t = 3.0$ μs, $t = 3.5$ μs, and $t = 4.0$ μs, and Figures 3(a) to 3(f) correspond to $t = 6.0$ μs, $t = 8.8$ μs, $t = 13.6$ μs, $t = 16.6$ μs, $t = 25.6$ μs, and $t = 41.6$ μs. In Figure 2(a), at $t = 1.5$ μs, the bubble has already collided with the vertical shock initially located at $x = 7.0$ mm. The bubble is pressed against denser hot air and a reflected wave appears on the right of the initial shock followed by expansion waves. On the left—upstream—side, there is a refracted wave inside the bubble, connected to a transmitted wave at the bubble interface. The transmitted wave is also connected tangentially to the reflected wave. The next Figures 2(b) and 2(c) illustrate the propagation of these various waves. In these Figures, the arrows indicate some of the waves moving during the interaction. A focusing wave first appears in the bubble as indicated by an arrow in Figure 2(b). The refracted wave separates from the left part of the hydrogen bubble between $t = 2.0$ μs and $t = 2.5$ μs. The shock compresses the diffusion interface between $t = 1.5$ μs and $t = 2.0$ μs but later the interface thickens thanks to diffusive processes. In Figure 2(c), the refracted and transmitted waves reconnect and exit on the left of the bubble. There is then a secondary vertical transmitted wave, an internal vertical reflected wave moving to the right, and the previous focusing wave is still going from the top to the symmetry line of the bubble.

At this stage, negative vorticity has already been accumulated in the upper and right sides of the distorted bubble interface. Indeed, when the shock interacts with the hydrogen bubble interface, vorticity is produced when the gradients of pressure and density are misaligned. The baroclinic production term $(1/\rho^2)\boldsymbol{\nabla}\rho \wedge \boldsymbol{\nabla}p$ becomes very high thanks to large density and pressure gradients and to the small value of the hydrogen density ρ. The upper right and right part of the bubble interface—the only part of the interface that have interacted with the shock and that are located around the apex of the bubble at $(7, 2.8)$ in mm—then become vorticity layers.

In Figure 2(d), the internal vertical reflected wave crosses the right interface of the distorted bubble, and develops a shock and expansion waves in air as illustrated in Figures 2(e) and 2(f). Simultaneously, there is a reflection at the bubble symmetry line of the wave going downward, leading to an important wave moving upward indicated by an arrow. If we take into account the lower part of the bubble, in the negative y domain, obtained by symmetry, the downward wave is then in the lower part of the bubble

and the upward wave is the wave coming from this lower part of the bubble. This upward wave yields a downward oriented pressure gradient which is misaligned with the right oriented density gradient at the right bubble interface, and the left oriented density gradient at the left bubble interface. The baroclinic vorticity production term $(1/\rho^2)\boldsymbol{\nabla}\rho \wedge \boldsymbol{\nabla}p$ becomes again very large with negative values on the right interface and positive values on the left interface. The amplitude of the upward wave is relatively weak, with $\Delta p \approx 25000$ pa compared to the initial pressure jump across the shock $\Delta p_{shock} \approx 350000$ pa, but the factor ρ^{-2} is larger since temperature is around 1400 K in the bubble as compared to 1000 K initially. In addition, for the right interface, negative vorticity adds up to the one already produced in the initial stage. As a result, negative vorticity is again stored along the right interface, especially between $t = 3$ μs and $t = 4$ μs in Figures 2(d) to 2(f), and a peak of negative vorticity appears on the right interface, near the point $x = 7$ mm, $y = 1.8$ mm, that will dominate the flow around the bubble. A vortex sets up in this region, begins to absorb the neighbouring vorticity of the same sign and consequently raises its global intensity. Some other secondary vortices arise and are progressively absorbed by the main vortex. The positive vorticity production, at the left distorted bubble interface, is not as high in absolute value as the negative vorticity production. This is due to smaller values of the pressure gradient and to the angle between pressure and density gradients. Nevertheless, positive vorticity accumulates along the left interface in Figures 2(d) to 2(f) and this will later influence the flow inside the bubble.

In Figures 2(e) and 2(f) we also note that the right vertical oriented shock in air—created by the internal reflected wave—has strenghened and is more sharp in comparison with the former internal wave in the hydrogen bubble. This can be attributed to the differences in the volume viscosity coefficients and in the sound velocities between hydrogen and air. The sound velocity is indeed lower in air—because it is a heavier gas—so that the waves emerging from the bubble automatically stiffen and strenghen. In Figures 2(e) and 2(f) the upward propagating wave inside the hydrogen bubble is connected to the right propagating shock in air and to a bent shock on the left. These three connected waves separate from the bubble in Figure 2(f). Up to Figure 2(f), the main variations in hydrogen concentration are still associated with fluid motion and not yet to combustion.

In Figure 3(a), the main vortex has started to pull the remaining part of the bubble nearby the symmetry axis. The two nearly vertical interfaces of this central thinner part of the bubble contain vorticity, positive on the left and negative on the right. These interfaces are strained, pulled, and made closer by the main vortex and the flow deceleration on the right of the interface. A secondary vortex also appears and will be absorbed by the main vortex. We can also see a circular shock, that was emerging in Figure 2(f), that is now propagating to the right and upward. In Figure 3(b) the main vortex has pulled part of the central region of the bubble, between the two thin interface layers, and the remaining part has been burnt in a double diffusion flame. Inside the resulting pocket of remaining hydrogen there is now a jet of denser gas. In addition, the former right interface has created a vortex of negative sign, whereas the former left interface has created a vortex of positive sign. The resulting motion inside the pocket is therefore mushroom shaped. These vortices are gradually absorbed by the main vortex as can be seen in Figure 3(c). In Figures 3(c), 3(d) and 3(e), the main vortex is then straining the remaining upper part of the bubble in a spiral until it is completely wrapped in Figure 3(f). In these Figures, we also see that combustion has gradually started. Hydrogen is first consumed inside the mushroom and next in the strained bubble as we will see by examining the temperature and species mass fractions fields.

6.3 Temperature and other species mass fraction

In Figures 4(a) to 4(f) are presented the isotherms at various times. Going from left to right and top to bottom, Figures 4(a) to 4(f) correspond to $t = 1.5$ μs, $t = 6.0$ μs, $t = 8.8$ μs, $t = 13.6$ μs, $t = 25.6$ μs, and $t = 41.6$ μs. In Figure 4(a), at time $t = 1.5$ μs, the bubble has started to interact with the shock. Temperature is 1000 K upstream of the refracted and transmitted shocks, and is around 1200 K inside of the remaining part of the bubble. Right of the bubble, the temperature rises from 1200 K up to the uniform downstream temperature $\simeq 1557$ K. There is only a slight temperature increase nearby the reflected shock of about 1715 K. At time $t = 6.0$ μs, presented on Figure 4(b), temperature has increased up to $\simeq 1400$ K inside the bubble, and the vertical right oriented shock—that is now propagating in air—has also heated up to 1600 K a significant part of the air right of the distorted bubble. Around this time, combustion starts to play its fundamental role and diffusion flames form where hot hydrogen and air meet. This can be seen on Figure 4(c) where ignition has taken place in the thin layer of hydrogen that was present nearby the symmetry line. This thin hydrogen layer is now burning as can be seen

on Figure 4(c) and temperature is much higher in this thin combustion layer. The mechanisms that ignited this thin layer are the higher temperatures due to the right propagating shock and the flow motion that forced the two bubble interfaces to get very close, leading to high concentration gradients, enhanced diffusion, and enhanced fuel and air mixing. On Figure 4(d), ignition has now taken place around every hydrogen/air interface and the hot temperature zone follows the motion imposed by the main vortex and by thermal conductivity as can be seen on Figures 4(e) and 4(f).

In Figures 5(a) to (f) we present respectively the vorticity and the H_2O, O, HO_2, OH, and H mass fractions isopleths at time $t = 13.6$ μs. In each of these species plots we have also indicated the H_2 mass fraction contours in black color in order to locate the remaining part of the hydrogen bubble. The corresponding pressure isocontours, H_2 mass fraction isopleths, and isotherms are presented respectively in Figures 3(c) and 4(d). Aside from the inert pocket of pure hydrogen indicated in Figure 3(c), three different zones can be identified from a chemistry point of view. There is first the remaining part of the double diffusion flame nearby the symmetry axis which is progressively extinguishing. There is then the core of the dominating vortex which is rather cold and is constituted by a mixture of fresh air, unburnt hydrogen, and products from the combustion of the former double diffusion flame layer. Finally, there is the envelope of both the vortex and the pure hydrogen pocket.

Nearby the symmetry axis, even if there is no more hydrogen, and no more atomic hydrogen H, water vapor is present as well as active radicals like O, HO_2, and OH. The corresponding former double diffusion flame is progressively extinguishing due to the burning of all available fuel. In the core of the vortex, there is unburnt hydrogen, and active radicals like HO_2. The core of the vortex is therefore slowly igniting but its temperature is too low to allow for the self catalytic hydrogen combustion. The ignition process is still dominated by the formation of the HO_2 radical. From a reactive point of view, the most active zone is the envelope between the vortex plus the pure hydrogen pocket and the surrounding air. In this envelope, there is now a well established diffusion flame which produces water vapor and active radicals like O, HO_2, OH, and H. The very light atomic hydrogen radical H has already diffused all around the envelope diffusion flame. Around the pure hydrogen pocket, the OH and H radicals are very close to the hydrogen envelope. On the other hand, the radical HO_2 is farther from the hydrogen pocket envelope as could be expected since H destroys HO_2 at moderate to high temperatures. At later times, the pure hydrogen pocket is gradually rolled around the vortex and finally ignites and gradually burns around $t = 40$ μs.

7 Impact of Bulk viscosity

7.1 Shock thickness

In order to measure the impact of volume viscosity on shock structures, we have first plotted the pressure isocontours at time $t = 3.5$ μs on Figure 6(a). In this plot, the upper part corresponds to a numerical simulation with the volume viscosity, whereas the lower part corresponds to the same numerical simulation in the absence of volume viscosity, that is, with $\kappa = 0$. For all the shocks that are in air, where κ is not large, we obtain approximately similar results with or without volume viscosity. It is not the case, however, for the various reflected shocks in hydrogen, especially for the upward propagating shock (upward for $y > 0$ and downward for $y < 0$). These shocks are fairly weak and, in this situation, they are significantly thickened by volume viscosity, in agreement with the theoretical results of Section 4.3. In order to have a closer look at the shock structure, we have plotted the pressure along the two pathes indicated by $c1$ and $c2$ in Figure 6(b). The line $c1$ is along the x axis and crosses twice the hydrogen bubble interface. The broken line $c2$ is in the core of the hydrogen bubble and crosses in particular the important upward propagating shock.

The pressure curves along $c1$ are given in Figure 6(c). These curves clearly show that in air the shocks are nearly identical with or without volume viscosity, but this is not the case in hydrogen. Indeed, in the hydrogen bubble, we see an important difference in the shock structure, with a much thicker shock when volume viscosity is taken into account, in agreement with the asymptotic theory of shock internal structure. This effect is more dramatic in Figure 6(d) where we have plotted the pressure along the broken line $c2$. We see that the upward propagating shock is much smoother when volume viscosity is taken into account.

From a quantitative point of view, we do not expect any one dimensional steady calculation—and a fortiori the simplified Taylor asymptotic expansion—to be accurate for predicting the slope ratio between the pressure plots with and without volume viscosity. Indeed, in our time dependent multidimensional calculation, there are unsteady effects, the profiles ahead and downstream of the

shocks are not flat, there are two dimensional curvature effects, eventually mixing and reaction effects and Taylor formula is only an asymptotic—not an exact—formula. Nevertheless, the maximum slope ratio is approximately ≈ 2.96 around $x \approx 5.25$ mm in Figure 6(c) and is approximately ≈ 3.71 around $y \approx 2.44$ mm in Figure 6(d). The corresponding weak shocks are thus much thicker when volume viscosity is taken into account.

The thickness of the upward propagating shock in the hydrogen bubble is a key point to understand the impact of volume viscosity. More specifically, when volume viscosity is taken into account, this shock is much smoother in agreement with the physical theory of shock internal structure. As a consequence, the baroclinic vorticity production term $(1/\rho^2)\boldsymbol{\nabla}\rho \wedge \boldsymbol{\nabla}p$ is lower than in absence of volume viscosity. Therefore, the vorticity stored in the left and right interfaces are different with or without κ. With volume viscosity, vorticity production is more diffuse, so that the vorticity distribution differs from that without κ. Since vorticity effects are dominating the flow motion during the shock/bubble interaction, we expect the vorticity to be different until vorticity diffusion smoothes out all these effects. In summary, κ modifies the shocks in the hydrogen bubble, the pressure gradients are thus modified, the vorticity is thus modified, all the flow structure is perturbed, and the flame structure is changed.

7.2 Species mass fractions

In Figure 7(a) we have plotted the H_2 mass fraction isopleths at $t = 21.6$ μs computed with the volume viscosity on the upper part and without the volume viscosity on the lower part. It is readily seen that the volume viscosity has an important impact on the fuel distribution inside the bubble. This distribution is different because of the difference in flow motion that has led to the wrapping of fuel layers around the main vortex. The differences in the vorticity distribution due to κ have created—after some time—large differences in the fuel distribution. It is important to note that this effect is strictly multidimensional since it is due to the baroclinic term. When numerical simulations are performed in one dimension, the differences between two simulations including or not the volume viscosity are restricted to pressure variations into the hydrogen layer. Similar differences can be found in Figure 7(b) where we have plotted the water mass fraction isopleths. On Figure 7(c), the HO_2 radical is less sensitive since it is only present in the core and in the envelope of the central vortex and the pure fuel pocket. Nevertheless, its concentration in the core is affected with the volume viscosity. Finally, In Figure 7(d) we have presented the isotherms. The temperature field is also affected by the flow inside the central vortex. In particular, the maximum temperature are clearly different with $T \approx 2422K$ when $\kappa \neq 0$ and $T \approx 2467K$ when $\kappa = 0$, and space distribution of temperature is different.

7.3 Influence of barodiffusion

In our simulations, we have also investigated the influence of barodiffusion. The diffusion driving force of the i^{th} species—given in Equation (15)—can indeed be decomposed into a mole fraction gradient $\boldsymbol{\nabla}X_i$ and a barodiffusive term $(X_i - Y_i)\boldsymbol{\nabla}\log p$. This term is usually negligible for low Mach number combustion. However, when a shock crosses a mixture whose species have very different molar masses, as in a H_2-air flame for instance, this term may no longer be negligeable. More specifically, we have performed numerical simulations with and without the barodiffusion terms $(X_i - Y_i)\boldsymbol{\nabla}\log p$. We have then measured mass fraction differences as high as 20% mainly due to little shifts in the front locations. Therefore, this term must be taken into account for the numerical simulation of fast flows.

7.4 Influence of thermodiffusion

The Soret effect accounts for the diffusion of mass due to temperature gradients. This effect tends to drive light molecules towards hot regions and heavy molecules towards cold regions. It is usually important in premixed flames, particularly for hydrogen combustion and, more generally, for reactive flows where light radicals like H or H_2 play a major role. However, in the shock/bubble interaction, the temperature differences are not very high initially, since the temperature jump across the shock is only $\Delta T \approx 500K$, and it does not perturb the reactive species distribution. We have indeed found that the Soret and Dufour effects are negligible in the simulations, especially compared to the barodiffusive term.

8 Conclusion

Theoretical calculations and experimental measurements have shown that the ratio κ/η is not small for polyatomic gases. Volume viscosity also arises in dense gases and in liquids, and its absence in dilute monatomic gases is an exception rather than a rule. We have established, however, that in a number of situation, the whole term $\boldsymbol{\nabla}\cdot\big(\kappa(\boldsymbol{\nabla}\cdot\boldsymbol{v})\boldsymbol{I}\big)$ can be neglected because of its *structure*, even though both the ratio κ/η and the dilatation $\boldsymbol{\nabla}\cdot\boldsymbol{v}$ are not necessarily small. This is the case, in particular, for small Mach number flows and classical boundary layer flows.

We have shown, however, that volume viscosity has an important impact during a shock/hydrogen bubble interaction. Volume viscosity modifies pressure gradients in hydrogen and thus vorticity production. The whole flow structure is then modified, especially the internal structure of the dominating vortex during the transient phase, where nonlinear processes are preponderant. The volume viscosity coefficient should therefore systematically be included in direct numerical simulations of reactive fast flows.

Références

[1] R. Abgrall, T. Sonar, O. Friedrich, G. Billet, 'High order approximations for compressible fluid dynamics on unstructured and cartesian meshes', High-Order Methods for Computational Physics, Lecture Notes in Computational Science and Engineering, Springer, (1999).

[2] R. Abgrall , S. Karni, 'Compressible multifluids' J. Comput. Phys., 169, pp 594-623, (2001).

[3] H. Alsmeyer, 'Density Profiles in Argon and Nitrogen Shock Waves measured by the Absorption of an Electron beam' J. Fluid Mech., 74, pp 497–513, (1976).

[4] M. Baum, T. Poinsot, D. Thévenin, 'Accurate boundary conditions for multicomponent reactive flows' J. Comput. Phys., 116, pp 247–261, (1994).

[5] H. Bongers and L.P.H. de Goey, 'The effect of simplified transport modeling on the burning velocity of laminar premixed flames' Comb. Sci. Tech., 175, pp 1915–1928, (2003).

[6] R. Bendahklia, V. Giovangigli, and D. Rosner, 'Soret effects in laminar counterflow spray diffusion flames' Comb. Theory Mod., 6, pp 1–17, (2002).

[7] G. Billet, O. Louédin, 'A simple algorithm to improve the accuracy of TVD-MUSCL schemes' Inter. Series Num. Math., 129, pp 65–75, (1999).

[8] G. Billet, O. Louédin 'Adaptive limiters for improving the accuracy of the MUSCL approach for unsteady flows' J. Comput. Phys., 170, pp 161–183, (2001).

[9] G. Billet, R. Abgrall, 'An adaptive shock-capturing algorithm for solving unsteady reactive flows' Comput. & Fluids, 32, pp 1473–1495, (2003).

[10] G. Billet, 'Improvement of convective concentration fluxes in a one step reactive flow solver' J. Comput. Phys., 204, pp 319-352, (2005).

[11] M. Borrel, J. Ryan and G. Billet, 'A Generalized Patch AMR Platform that uses Celle Centered or Cell Vertex Solvers', ECCOMAS CFD 2006, Delft, Netherland, (2006).

[12] S. Chapman and T.G. Cowling, 'The Mathematical Theory of Non-Uniform Gases', Cambridge University Press, (1970).

[13] C. Cercignani, 'The Boltzmann Equation and its Applications', Applied Mathematical Sciences, 67, Springer Verlag, New York, (1988).

[14] W.S. Don, C.B. Quillen, 'Numerical simulation of shock-cylinder interactions, I. Resolution' J. Comput. Phys., 122, pp 244–265, (1995).

[15] G. Emanuel 'Bulk viscosity of a dilute polyatomic gas' Phys. Fluids, A, 2, pp 2252–2254, (1990).

[16] G. Emanuel, 'Effect of bulk viscosity on a hypersonic boundary layer' Phys. Fluids, A, 4, pp 491–495, (1992).

[17] A. Ern and V. Giovangigli, 'Multicomponent Transport Algorithms' Lecture Notes in Physics, New series Monographs m24, (1994).

[18] A. Ern and V. Giovangigli, 'Volume viscosity of dilute polyatomic gas mixtures' Eur. J. Mech., B/Fluids, 14, pp 653–669, (1995).

[19] A. Ern and V. Giovangigli, 'Fast and accurate multicomponent transport property evaluation' J. Comp. Phys., 120, pp 105–116, (1995).

[20] A. Ern and V. Giovangigli, 'Optimized transport algorithms for flame codes' Comb. Sci. Tech., 118, pp 387–395, (1995).

[21] A. Ern, V. Giovangigli, 'EGlib server and User's manual' http ://www.cmap.polytechnique.fr/www.eglib.

[22] A. Ern and V. Giovangigli, 'Thermal Diffusion Effects in Hydrogen-Air and Methane-Air Flames', Comb. Theory Mod., 2, pp 349–372, (1998).

[23] A. Ern and V. Giovangigli, 'Impact of multicomponent transport on planar and counterflow hydrogen/air and methane/air flames', Comb. Sci. Tech., 149, pp 157–181, (1999).

[24] A. Ern, V. Giovangigli and M. Smooke, 'Numerical Study of a Three-Dimensional Chemical Vapor Deposition Reactor with Detailed Chemistry', J. Comp. Phys., 126, pp 21–39, (1996).

[25] J.H. Ferziger, H.G. Kaper, 'Mathematical theory of transport processes in gases', North Holland, Amsterdam, (1972).

[26] P. Garcia-Ybara, C. Nicoli, and P. Clavin , 'Soret and dilution effects on premixed flames' Comb. Sci. Tech., 42, pp 87–109, (1984).

[27] V. Giovangigli, 'Multicomponent flow modeling', Birkhaüser, Boston, (1999).

[28] V. Giovangigli V and N. Darabiha, 'Vector Computers and Complex Chemistry Combustion' *Mathematical Modeling in Combustion and Related Topics* (Brauner C and Schmidt-Laine C Eds. Nijhoff M Pug.) NATO ASI Series, 140, pp. 491–503, (1988).

[29] D. Gilbarg and D. Paolucci, 'The Structure of Shock Waves in the Continuum Theory of Fluids' J. Rat. Mech. Anal., 2, pp 617–642, (1953).

[30] R. E. Graves and B. Argrow, 'Bulk viscosity : past to present' Journal of Thermophysics and Heat Transfer, 13, pp 337–342, (1999).

[31] J.F. Haas, B. Sturtevant, 'Interaction of weak shock waves with cylindrical and spherical gas inhomogeneities' J. Fluid Mech., 181, pp 41-76, (1987).

[32] R.D. Hancock, F.R. Schauer, R.P. Lucht, V.R. Katta, and K.Y. Hsu, 'Thermal diffusion effects and vortex-flame interactions in hydrogen jet diffusion flames' Proc. Combust. Inst., 26, pp 1087–1093, (1996).

[33] P.W. Hermans, L.F.J. Hermans, and J.J.M. Beenakker, 'A survey of experimental data related to the non-spherical interaction for the hydrogen isotopes and their mixture with noble gases' Physica A, 122, pp 173–211, (1983).

[34] R. Hilbert, F. Tap, H. El-Rabii, and D. Thevenin, 'Impact of Detailed Chemistry and Transport Models on Turbulent Combustion Simulations' Prog. Ener. Comb. Science, 30, pp 61–117, (2004).

[35] J.O. Hirschfelder, C.F. Curtiss, R.B. Bird, 'Molecular theory of gases and liquids', New-York, Wiley, (1954).

[36] S.M. Karim and L. Rosenhead, 'The second coefficient of viscosity of Liquids and gases', Reviews of Modern Physics, 24, pp 108–116, (1952).

[37] G.M. Kremer and I. Müller, 'Shock Thickness in Monatomic Gases', Mecanica, 32, pp 295–299, (1997).

[38] L.C. Landau and E.M. Liftshitz, 'Fluid Mechanics', Pergamon press, New York, (1959).

[39] M.S. Liou, 'A sequel to AUSM : AUSM$^+$ ' J. Comput. Phys., 129, pp 364–382, (1996).

[40] F.R. McCourt, J.J. Beenakker, W.E. Köhler, I. Kuscer, 'Non equilibrium phenomena in polyatomic gases, Volume I : Dilute gases, Volume II : Cross sections, scattering and rarefied gases' Clarendon Press, Oxford, (1990).

[41] J.A. Miller, R.E. Mitchell, M.D. Smooke, R.J. Kee, 'Toward a comprehensive chemical kinetic mechanism for the oxidation of acetylene : comparison of model predictions with results from flame and shock tube experiments', Proc. Combust. Inst., 19, pp 181-196, (1982).

[42] E.P. Muntz and L.N. Harnett, 'Molecular Velocity Distribution Function Measurements in a Normal Shock Wave' Phys. Fluids, 12, pp 2027–2035, (1969).

[43] J.M. Picone, J.P. Boris, 'Vorticity generation by shock propagation through bubbles in a gas' J. Fluid Mech., 189, pp 23–51, (1988).

[44] T.J. Poinsot and S.K. Lele, 'Boundary conditions for direct numerical simulation of compressible viscous flows' J. Comp. Phys., 101, pp 104–129, (1992).

[45] G.J. Prangsma, L.J.M. Borsboom, H.F.P. Knaap, C.J.N. Van den Meijdenberg, and J.J.M. Beenakker, 'Rotational relaxation in ortho Hydrogen between 170 and 300 K' Physica, 61, pp 527–538, (1972).

[46] G.J. Prangsma, A.H. Alberga, and J.J.M. Beenakker, 'Ultrasonic determination of the volume viscosity of N_2, CO, CH_4, and CD_4 between 77 and 300K' Physica, 64, pp 278–288, (1973).

[47] J.J. Quirk, S. Karni, 'On the dynamics of a shock-bubble interaction', NASA Icase Report 94-75, (1994).

[48] L. Monchick, K. S. Yun, and E. A. Mason, 'Formal Kinetic Theory of Transport Phenomena in Polyatomic Gas Mixtures', J. Chem. Phys., 39, pp. 654–669, (1963).

[49] D.E. Rosner, 'Thermal (Soret) diffusion effects on interfacial mass transport rates', PhysicoChemical Hydrodynamics, 1, pp 159–185, (1996).

[50] B. Sjögreen and H.C. Yee, 'Grid convergence of high order methods for multiscale complex unsteady viscous compressible flows' J. Comput. Phys., 185, pp 1-26, (2003).

[51] P.A. Thompson, 'Compressible-Fluid Dynamics', McGraw Hill, New York, (1972).

[52] G. I. Taylor, 'The Conditions Necessary for a Discontinuous Motion in Gases', Proc. Roy. Soc. London A, 11, pp 371–377, (1910).

[53] L. Tisza, 'Supersonic absorption and Stokes viscosity relation', Physical Review, 61, pp 531–536, (1941).

[54] A.F. Turfa, H.F.P. Knaap, B.J. Thijsse, and J.J.M. Beenakker, 'A classical dynamics study of rotational relaxation in nitrogen gases', Physical A, 112, pp 19–28, (1982).

[55] B. Van Leer, 'Towards the ultimate conservative difference scheme.V. A second order sequel to Godunov's method' J. Comput.Phys., 32, pp 101–136, (1979).

[56] L. Waldmann, E. Trübenbacher, 'Formale kinetische Theorie von Gasgemischen aus anregbaren molekülen' Zeitschr. Naturforschg., 17a, pp 363-376, (1962).

[57] F. A. Williams, 'Combustion Theory', The Benjamin/Cummings Publishing Company, Inc., Menlo Park, (1985).

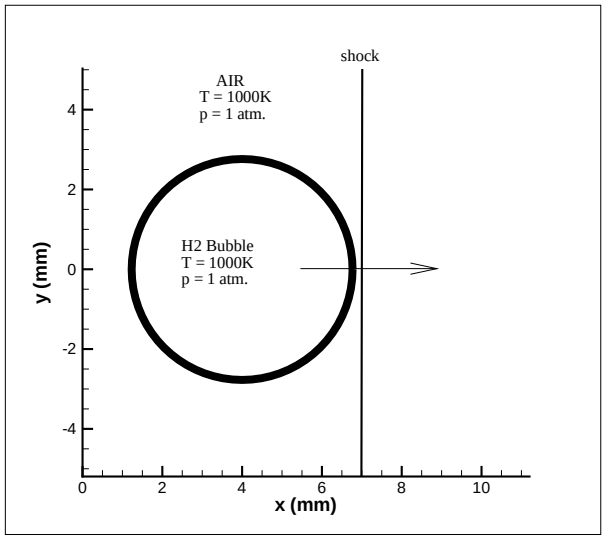

FIG. 1 – Schematic of the shock-bubble interaction.

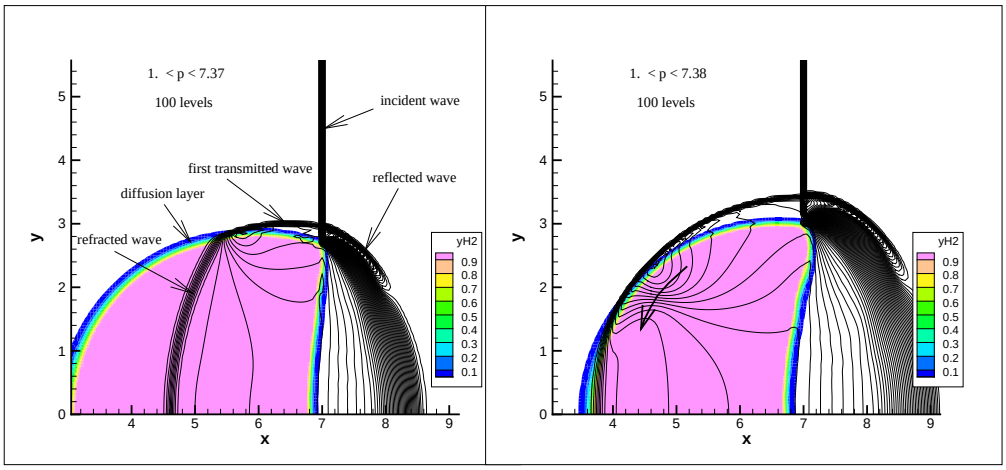

(a) $t = 1.5\ \mu$s

(b) $t = 2.0\ \mu$s

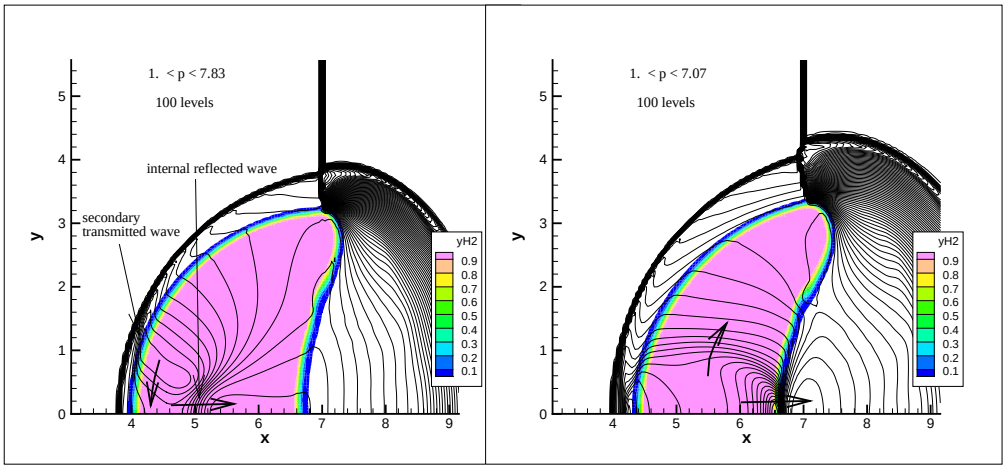

(c) $t = 2.5\ \mu$s

(d) $t = 3.0\ \mu$s

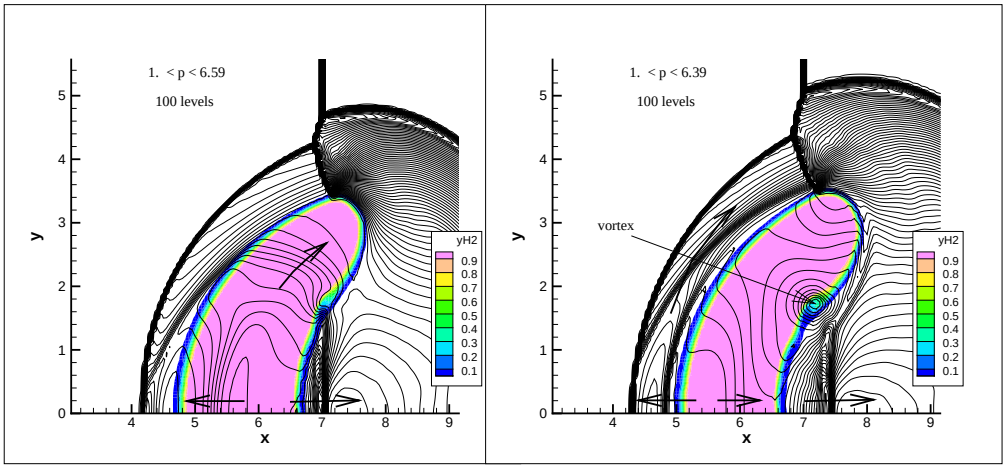

(e) $t = 3.5\ \mu$s

(f) $t = 4.0\ \mu$s

FIG. 2 – Pressure (atm) and hydrogen mass fraction isocontours at various instants.

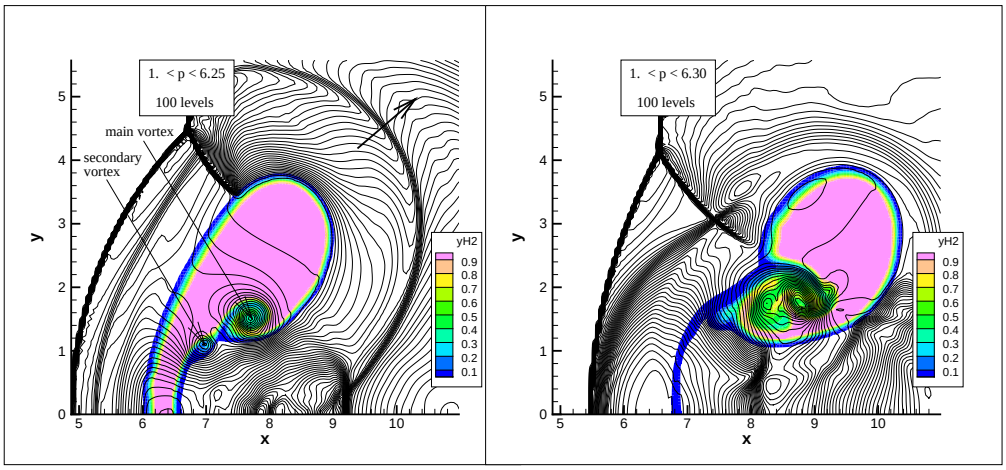

(a) $t = 6.0\ \mu$s

(b) $t = 8.8\ \mu$s

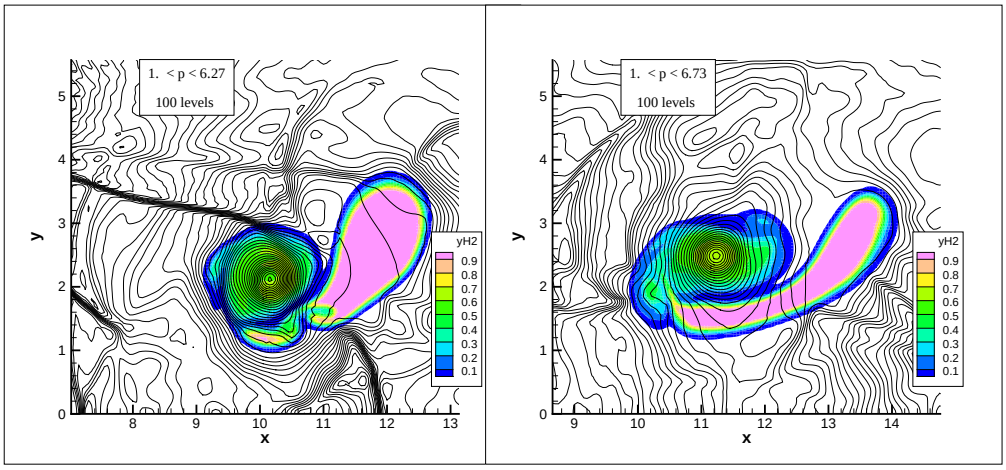

(c) $t = 13.6\ \mu$s

(d) $t = 16.6\ \mu$s

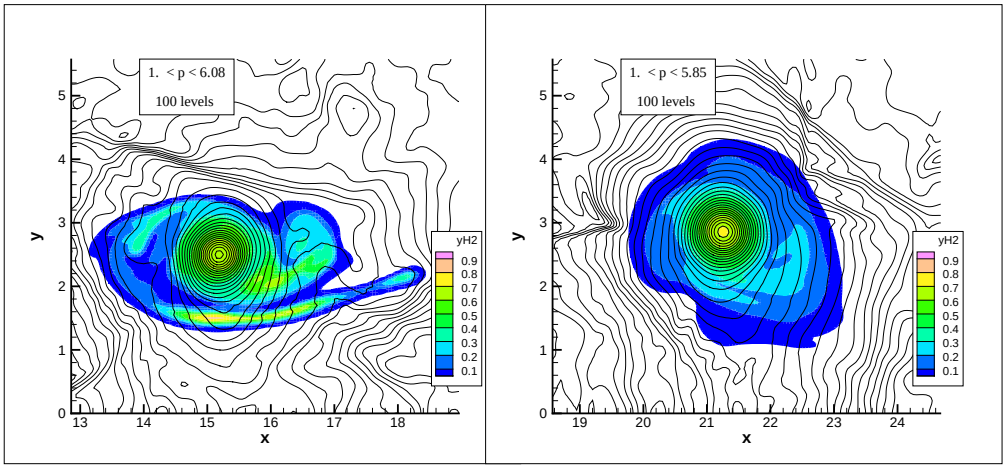

(e) $t = 25.6\ \mu$s

(f) $t = 41.6\ \mu$s

FIG. 3 – Pressure (atm) and hydrogen mass fraction isocontours at various instants.

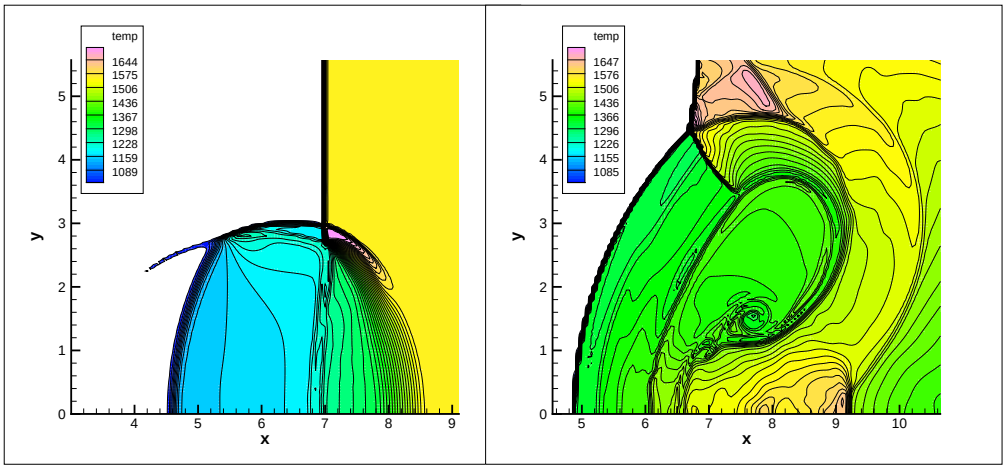

(a) $t = 1.5$ μs (b) $t = 6.0$ μs

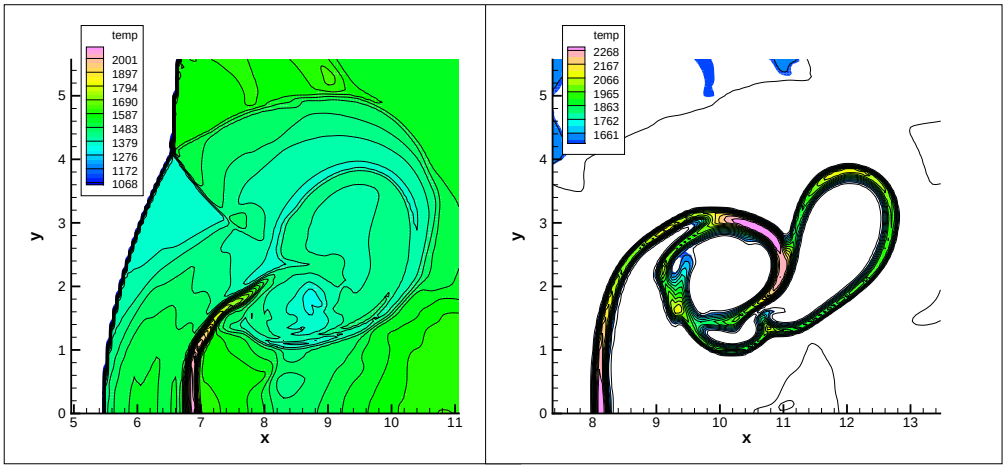

(c) $t = 8.8$ μs (d) $t = 13.6$ μs

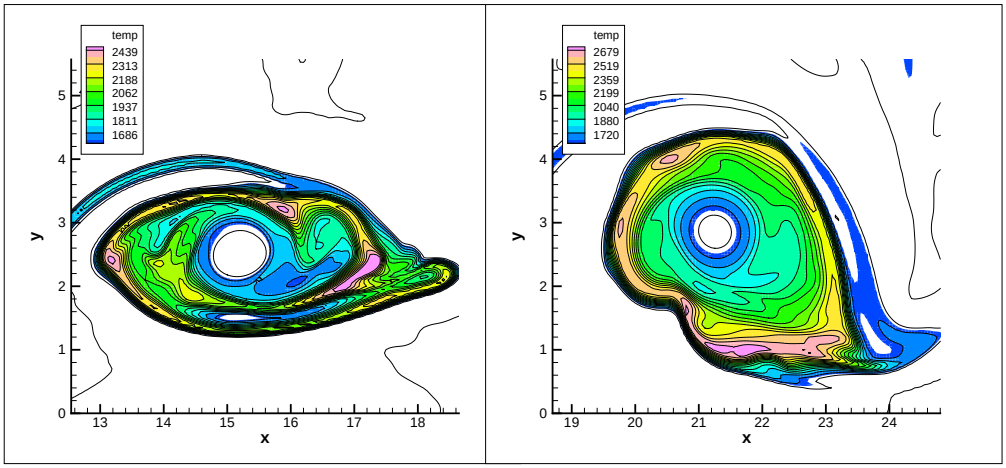

(e) $t = 25.6$ μs (f) $t = 41.6$ μs

FIG. 4 – Temperature isocontours at various instants.

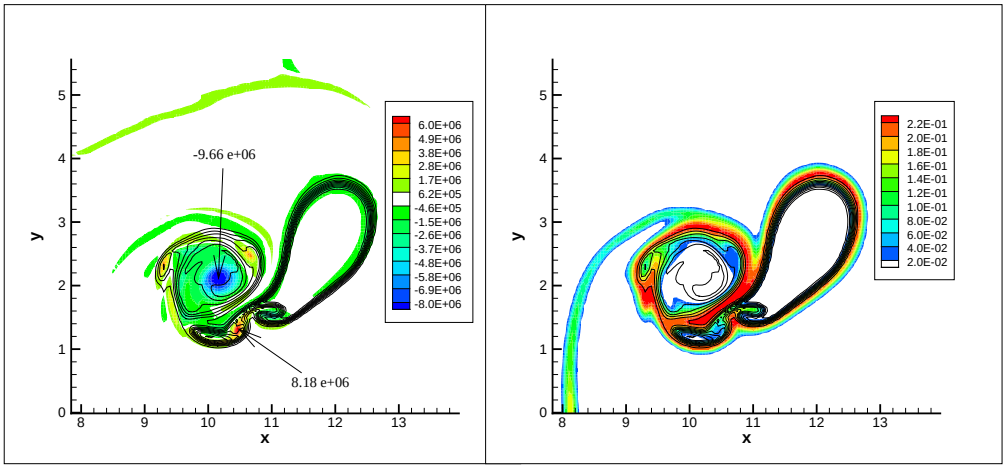

(a) Vorticity at $t = 13.6$ μs

(b) H_2O mass fraction at $t = 13.6$ μs

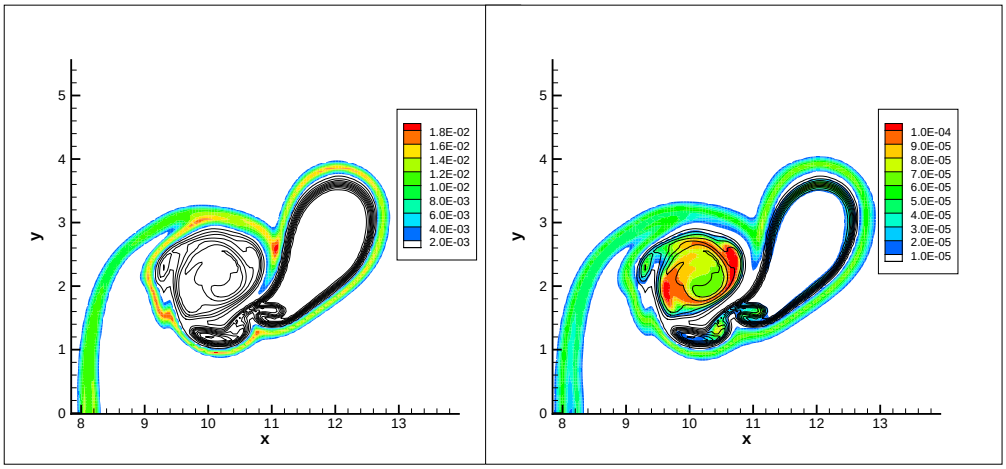

(c) O mass fraction at $t = 13.6$ μs

(d) HO_2 mass fraction at $t = 13.6$ μs

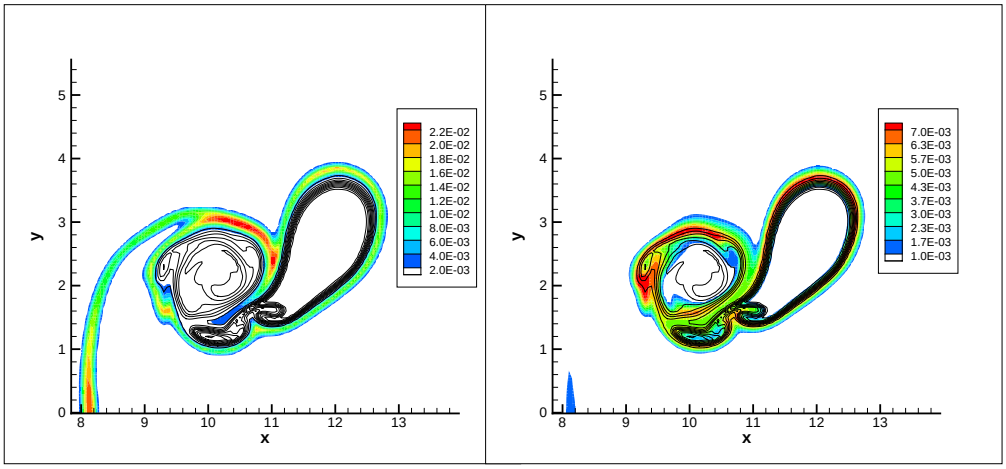

(e) OH mass fraction at $t = 13.6$ μs

(f) H mass fraction at $t = 13.6$ μs

FIG. 5 – Vorticity ($1/s^2$), and H_2O, O, HO_2, OH and H mass fractions at time $t = 13.6$ μs.

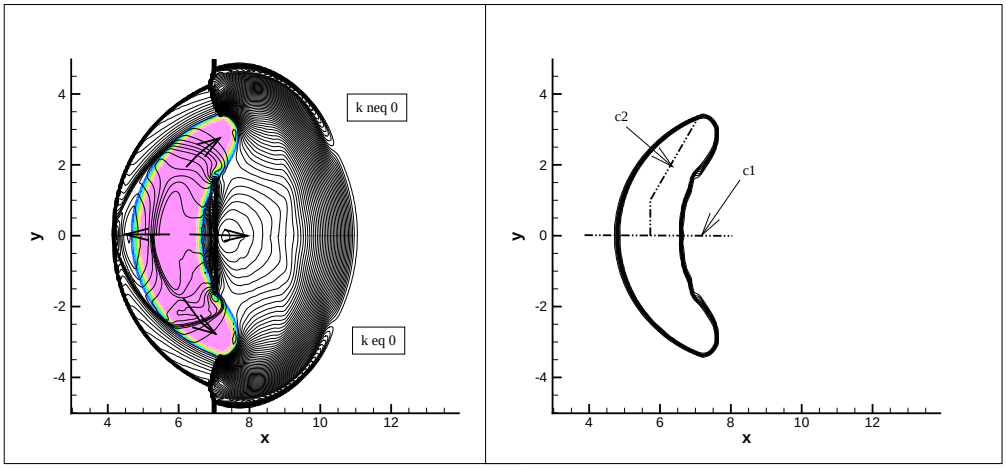

(a) Pressure isocontours at $t = 3.5$ μs (b) Lines for pressure plots at $t = 3.5$ μs

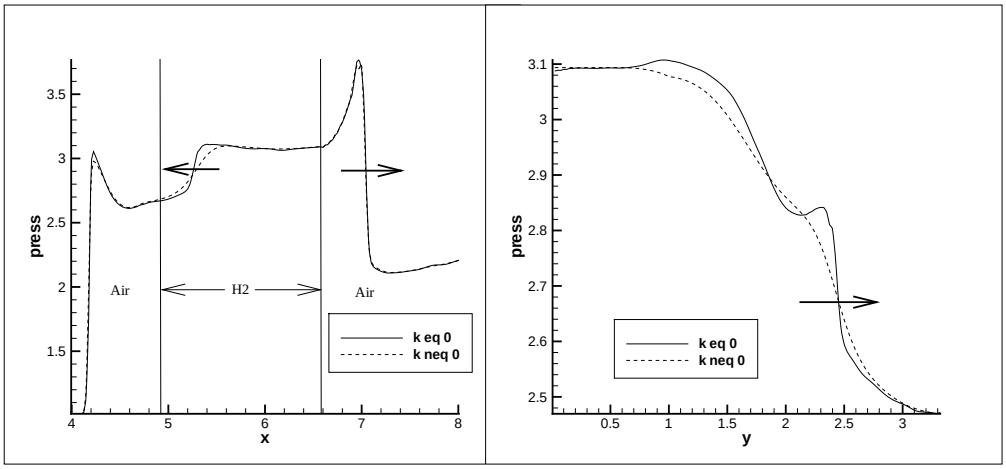

(c) Pressure along $c1$ at $t = 3.5$ μs (d) Pressure in the bubble along $c2$ at $t = 3.5$ μs

FIG. 6 – Influence of κ on shock wave thickness

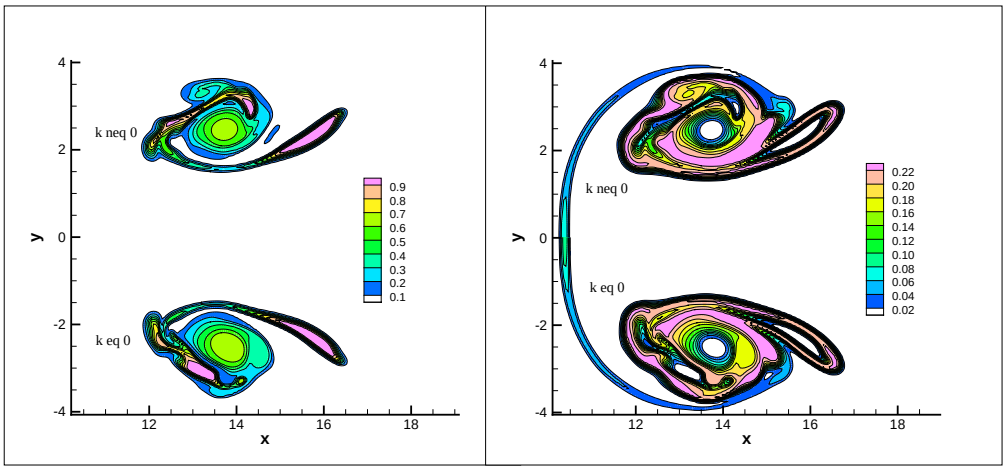

(a) H_2 mass fraction at $t = 21.6$ μs

(b) H_2O mass fraction at $t = 21.6$ μs

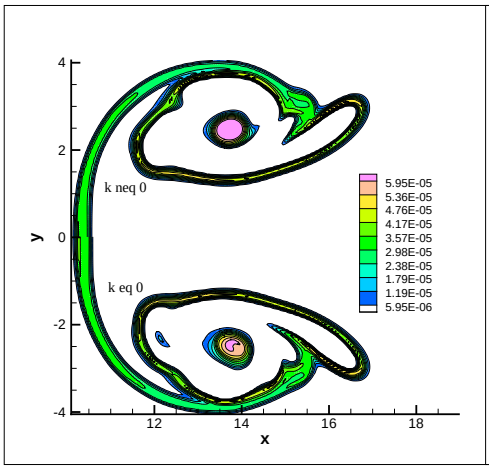

(c) HO_2 mass fraction at $t = 21.6$ μs

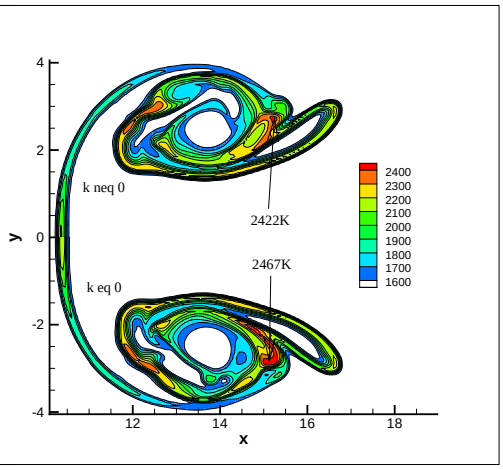

(d) Temperature at $t = 21.6$ μs

FIG. 7 – Impact of volume viscosity